Microscopic self-dynamics in liquid Ne-D_2 mixtures: Quantum features and itinerant oscillators reexamined

Daniele Colognesi [1,*] Ubaldo Bafile [1] Eleonora Guarini [2] and Martin Neumann [3]

[1] *Consiglio Nazionale delle Ricerche, Istituto di Fisica Applicata "N. Carrara", via Madonna del Piano 10, I-50019 Sesto Fiorentino, Italy*

[2] *Dipartimento di Fisica e Astronomia, Università di Firenze, via G. Sansone 1, I-50019 Sesto Fiorentino, Italy*

[3] *Fakultät für Physik der Universität Wien, Kolingasse 14-16, A-1090 Wien, Austria*

(Received 19 September 2023; accepted 20 March 2024; published 9 April 2024)

In this paper, we report the results of a centroid molecular dynamics (CMD) study of the canonical velocity autocorrelation functions (VACFs) in liquid Ne-D_2 mixtures at a temperature of $T = 30$ K and in the full D_2-concentration range ($0\% \leqslant x_{D_2} \leqslant 100\%$). This binary system was selected because of its moderate, although sizable, quantum effects which, as far as its equilibrium properties are concerned, are fully described by the path integral Monte Carlo (PIMC) simulations that have been also implemented. A comprehensive test of the VACF spectral moments carried out using three physical quantities (namely, mean kinetic energy, Einstein frequency, and mean-squared force) obtained from PIMC was performed revealing the potentialities, as well as the limitations, of the CMD approach to the single-particle dynamics in these low-T liquid mixtures. Additional physical information was extracted from the canonical VACFs by fitting their spectra via two distinct methods: the Levesque-Verlet model (LV, very flexible but highly heuristic) and the itinerant oscillator model (IO, based on the physical ground of a single particle rattling inside a short-lived diffusing pseudocage). Both provided good fits of the CMD outputs, with LV being always more adequate than IO in the case of the Ne VACFs, while, as for the D_2 VACFs, the LV superiority is evident only at high x_{D_2} values. However, a peculiar and systematic effect was found after analyzing the IO-fitted parameters: the estimated pseudocage masses turned out to be at least one order of magnitude lower than the corresponding values inferred from the PIMC simulations. This outcome concerns both the Ne and the D_2 rattling molecule and, as we also discovered, had already been observed (but promptly forgotten) in purely classical simulations of liquid Ar. The possible physical origins of this finding have been finally discussed in some detail, also in connection with the result of the more recent exponential expansion theory (EET), which manages to shed more light on the concept of single particles rattling inside short-lived pseudocages, ultimately demonstrating its untenability.

DOI: 10.1103/PhysRevE.109.045104

I. INTRODUCTION

Many of the current theories of liquid matter [1], even the most advanced, are based on concepts mainly related to classical statistical physics, with the notable exception of liquid helium [2–4]. This classical framework certainly originated from the fact that the temperature (T) range of existence of most liquids (i.e., that between the triple point temperature T_{tp} and the critical temperature T_c) is considered sufficiently distant from those low-T values where deviations from classical physics are known to occur. However, some liquids exhibit Debye temperatures [5], Θ_D, considerably higher than those of their respective triple points. For instance, in standard liquid hydrogen (i.e., at $T = 20.28$ K and ambient pressure [6]), one can roughly estimate $\Theta_D \approx 155$ K [7], while $T_{tp} = 13.80$ K [6]. Now, it is well-known that for $T < \Theta_D$ a many-body system cannot be considered as ruled by classical physics, since a large fraction of its collective excitations are still in their quantum ground state [8]. For this reason, various liquids, ranging from noble gases like Ne [9] to lightweight diatomic systems like H_2 [10] and even to water [11], obviously including (when existing) their intermixtures, actually exhibit a sizable quantum behavior affecting the equation of state, the macroscopic thermodynamical properties, the microscopic structure, as well as the transport coefficients and the related microscopic dynamic properties.

In what follows we will focus our study on a simple binary system (namely, the Ne-D_2 liquid mixture at $T = 30$ K and saturated vapor pressure) investigating both its microscopic structural features via the *static pair correlation functions* (SPCFs) [12], and its single-particle dynamic properties through the *velocity autocorrelation functions* (VACFs) [12] using quantum simulation techniques. As mentioned in a recent paper [13], the interest in this type of low-T liquid mixture is also motivated by the fact that the molecular parameters (i.e., σ and ϵ) of the Lennard-Jones potentials of deuterium and neon are very similar [14], so one can treat the Ne-D_2 solutions as "pseudoisotopic," getting rid of all the complications related to the variation of the interparticle potentials and focusing on the mass (M) of the two molecular species which influences the corresponding quantum properties. In this respect, since the mass ratio $M_{Ne}/M_{D_2} = 5.011$ is quite big, it is possible to isothermally control the size of

*d.colognesi@ifac.cnr.it

TABLE I. Thermodynamic conditions of the liquid samples simulated at $T = 30.0$ K and other details, including: simulation number "No.," total number of particles N, number of D_2 molecules N_{D_2}, deuterium concentration x_{D_2}, total molecular density n, Ne mean kinetic energy $\langle E_K \rangle_{Ne}$ per particle and D_2 mean kinetic energy $\langle E_K \rangle_{D_2}$ per particle (both from PIMC), Ne Debye temperature $\Theta_{D,Ne}$ and D_2 Debye temperature Θ_{D,D_2} (both from PIMC), Ne self-diffusion coefficient D_{Ne} and D_2 self-diffusion coefficient D_{D_2} (both from CMD). Statistical errors are reported in parentheses. See the main text for further details.

No.	N	N_{D_2}	x_{D_2} (%)	n (nm^{-3})	$k_B^{-1}\langle E_K \rangle_{D_2}$ (K)	$k_B^{-1}\langle E_K \rangle_{Ne}$ (K)	Θ_{D,D_2} (K)	$\Theta_{D,Ne}$ (K)	D_{D_2} (10^5 cm^2/s)	D_{Ne} (10^5 cm^2/s)
I	256	0	0.00	34.44	—	54.27(1)	—	62.40(4)	—	2.0279(6)
II	256	38	14.84	30.71	72.40(1)	52.70(1)	112.46(2)	56.64(4)	3.227(7)	2.8916(7)
III	256	64	25.00	28.60	69.52(1)	52.04(1)	105.60(2)	54.06(4)	4.208(5)	3.5543(7)
IV	256	90	35.16	26.80	67.09(1)	51.29(1)	99.60(3)	51.00(4)	5.192(5)	4.2783(9)
V	256	115	44.92	25.34	65.48(1)	50.81(1)	95.51(3)	48.96(4)	6.217(4)	5.063(1)
VI	256	128	50.00	24.67	64.66(1)	50.53(1)	93.38(3)	47.73(4)	6.759(4)	5.418(1)
VII	256	141	55.08	24.07	63.98(1)	50.24(1)	91.59(3)	46.43(5)	7.212(3)	5.865(1)
VIII	256	192	75.00	22.33	62.10(1)	49.54(1)	86.51(3)	43.13(5)	9.160(3)	7.488(2)
IX	256	218	85.16	21.80	61.43(1)	49.40(1)	84.64(3)	42.44(5)	9.932(3)	8.203(2)
X	256	256	100.00	21.41	60.90(1)	—	83.15(3)	—	10.948(3)	—

quantum effects by changing the deuterium concentration x_{D_2} from 0 to 1, obtaining in this way an impressive molecular volume change as large as 60.9% (see below for details). This molecular volume increase, which can be qualitatively explained through the more pronounced quantum delocalization of D_2 with respect to Ne, was already investigated in Ref. [13] pointing out that the x_{D_2} variation from 0 to 1 drives the VACF of the deuterium component from a sort of "solidlike" scenario, where pseudophononic excitations are clearly detectable, to a more "gaslike" situation, largely dominated by diffusional mechanisms. However, the cited previous characterization was essentially accomplished in a qualitative way, as a byproduct of a neutron scattering experiment of two Ne-D_2 mixture samples, but no specific VACF model was proposed to describe the quantum simulation data obtained. By contrast, in the present work we aim at tackling the problem much more quantitatively, utilizing a larger number of concentration values and, moreover, comparing the simulated VACFs with some of the theoretical models present in the literature. In particular, the mentioned "solidlike" scenario (i.e., at low values of x_{D_2}) simulated with the advanced methods developed in the last twenty years, allows us to revisit the physical problem of the so-called *itinerant oscillators* (IOs), which was discussed by Sears [15] in 1965, from a rigorous quantum perspective and fully including all the various anharmonic vibrational effects. This aspect is particularly interesting given the ubiquitous character of the IO model which can be actually found in various research areas [16]. As for the general subject of the microscopic dynamics in binary fluid mixtures with large mass differences between the composing particles, we have to point out that in the recent past various authors have investigated this topic, often attracted by the paradigmatic examples of Li-Pb and Li-Mg melted alloys [17–19] or gaseous He-Ne and liquid Kr-Ar mixtures [20–23], always dealt with and simulated in a purely classical framework. However, we have also to note that, with few exceptions containing VACF simulations [24,25], most of the mentioned work has been mainly focused on the complex collective dynamics of these disordered systems, rather than on their single-particle dynamical aspects, which were generally limited to the evaluation of the self-diffusion coefficients.

The rest of the present paper will be organized as follows: Sec. II will be devoted to the computational details concerning the quantum simulations performed on the Ne-D_2 mixtures under investigation, to extract both the partial SPCFs and the VACFs. In Sec. III, we will discuss the obtained results, and some key physical quantities derived from the static structural data will be related to their estimates obtained from the single-particle dynamic ones. In addition, a comparison between the VACF spectra of the present study and three selected theoretical models will be also provided. Finally, Sec. IV will deal with the conclusions of this study.

II. QUANTUM STATIC AND DYNAMIC SIMULATIONS

The starting point of the present study is the quantum simulation data set concerning various Ne-D_2 liquid mixtures (all performed at $T = 30.0$ K and saturated vapor pressure [26]) in the full range of concentrations. The related thermodynamic details are reported in Table I, where the sample number "No.," the total number of simulated molecules N, the number of D_2 molecules considered N_{D_2}, the deuterium concentration, and the total molecular density n are presented. As for the last quantity, this has been estimated using the thermodynamic data available in the literature, namely: Refs. [27,28] for pure liquid neon, Ref. [29] for pure liquid deuterium, and eventually Refs. [26,30] for the nonideal behavior of the Ne-D_2 liquid mixtures. In addition, the thermodynamic data presented in the last two references have been checked and extrapolated via the *path integral Monte Carlo* technique (PIMC) [31] performed in an isothermal-isobaric ensemble estimating n and its variation with x_{D_2}. Subsequently, more accurate standard (isochoric) PIMC simulations have been carried out on all the samples in Table I to extract the partial SPCFs, $g_{\alpha,\beta}(r)$, and the single-particle mean kinetic energies, $\langle E_K \rangle_\alpha$ (i.e., the mean kinetic energies per particle), with $\alpha, \beta =$ Ne or D_2. The calculation of the former functions has been implemented in the PIMC code as

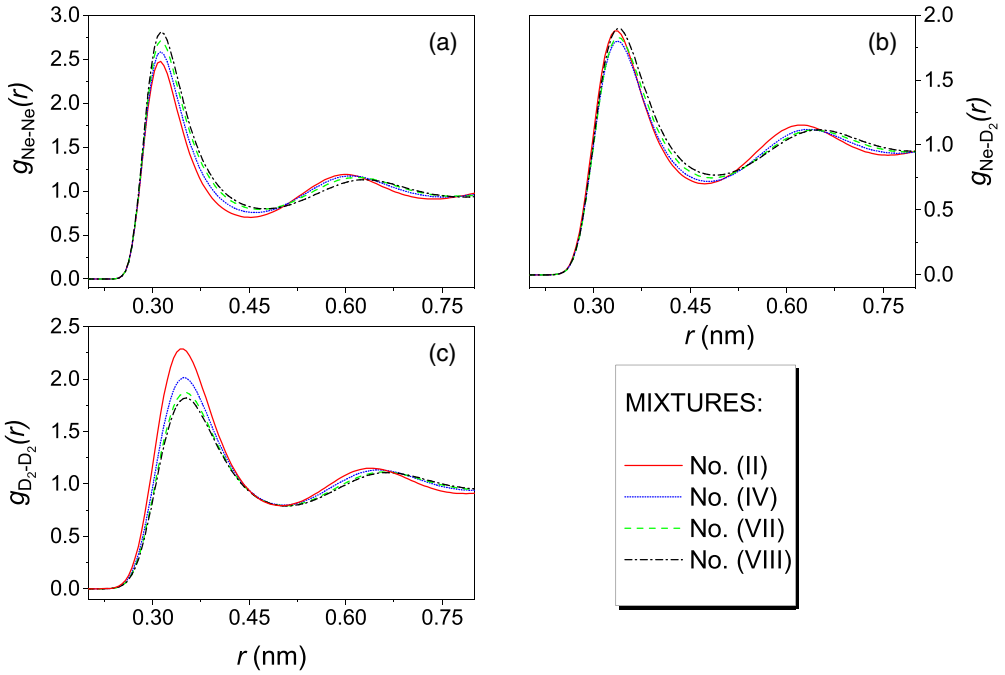

FIG. 1. Selected examples of the partial static pair correlation functions, $g_{\alpha,\beta}(r)$ (with $\alpha, \beta =$ Ne or D_2), obtained from path integral Monte Carlo simulations on four of the samples reported in Table I, namely No. II (red full line), No. IV (blue dotted line), No. VII (green dashed line), and No. VIII (black dot-dashed line). Panel (a) contains the $g_{Ne,Ne}(r)$ plots, panel (b) the $g_{Ne,D_2}(r)$ plots, and panel (c) the $g_{D_2,D_2}(r)$ ones.

follows [32]:

$$g_{\alpha,\alpha}(r) = \frac{V}{N_\alpha^2}\sum_{i=1}^{N_\alpha}\sum_{j\neq i}^{N_\alpha}\langle\delta(\mathbf{r}-\mathbf{r}_i+\mathbf{r}_j)\rangle,$$

$$g_{\alpha,\beta\neq\alpha}(r) = \frac{V}{N_\alpha N_\beta}\sum_{i=1}^{N_\alpha}\sum_{j=i}^{N_\beta}\langle\delta(\mathbf{r}-\mathbf{r}_i+\mathbf{r}_j)\rangle, \qquad (1)$$

where V is the volume of the simulation box and N_α (or N_β) represents the number of α-type (or β-type) molecules. In both PIMC versions the value of the Trotter number P (which in the "classical path integral isomorphism" replacing each quantum particle by a classical, harmonically bound ring polymer, represents the number of monomers) was set to 32. Tests with $P = 64$ showed no significant differences with respect to the previous case (see Appendix A for details). As for the total number of molecules, the PIMC simulations have been mainly performed with $N = 256$. Duplicating the simulations of sample No. II with twice the number of particles ($N = 512$) showed that there are only negligible finite-size effects on the quantities derived from the SPCFs as explained in Appendix A. Some selected examples of $g_{Ne,Ne}(r)$, $g_{Ne,D_2}(r)$, and $g_{D_2,D_2}(r)$ are reported in Fig. 1, where it is worth recalling that symbol "D_2" always refers to the molecular *center-of-mass* (CoM), rather than the individual nuclear positions, as will be made clear below in this section. As for the estimates of the mean kinetic energies, $\langle E_K\rangle_{Ne}$ and $\langle E_K\rangle_{D_2}$, these values are also reported in Table I.

Moving to the dynamic computational technique, we decided to employ the so-called centroid molecular dynamics (CMD) algorithm [33], which is based on an essentially exact quantum mechanical static distribution, while its dynamics is purely classical. In this approximation, the aforementioned "classical isomorphism" of PIMC is taken literally and the polymer centers (also known as "centroids") are allowed to evolve classically in a force field averaged over all the possible monomer positions. Observables and correlation functions are evaluated at the centroids' positions. From a practical point of view, CMD is a computational tool able to provide excellent approximations of the canonical (also known as "Kubo-transformed") correlation functions in many-body systems exhibiting mild quantum effects at nonzero temperature, when these functions include operators which are linear either in the coordinates or in the momenta of the particles composing the system [34]. Fortunately, this is exactly the case as far as canonical VACFs are concerned. Here it is probably worthwhile to recall the concept of the Kubo transform [35], $c_{AB}^{(K)}(t)$, of a generic time correlation function $c_{AB}(t)$ involving quantum operators $\hat{A}$ and $\hat{B}$. This transform is given by

$$c_{AB}^{(K)}(t) = \beta^{-1}\int_0^\beta c_{AB}(t+i\hbar\lambda)d\lambda, \qquad (2)$$

where $\beta = (k_B T)^{-1}$, with k_B being the Boltzmann constant.

Our CMD simulations have been performed with a timestep of $\Delta t = 0.005$ ps in the isokinetic ensemble where our velocity correlation functions were calculated up to a maximum time lag of 5 ps and averaged over 10 independent runs of 500 ps each at every thermodynamic state in Table I. For the total number of molecules and the Trotter number, we chose $N = 256$ and $P = 32$, identically to the PIMC case. Also in this case, tests with larger values of N and P (namely, $N = 1024$ and $P = 64$) have been carried out on sample No.

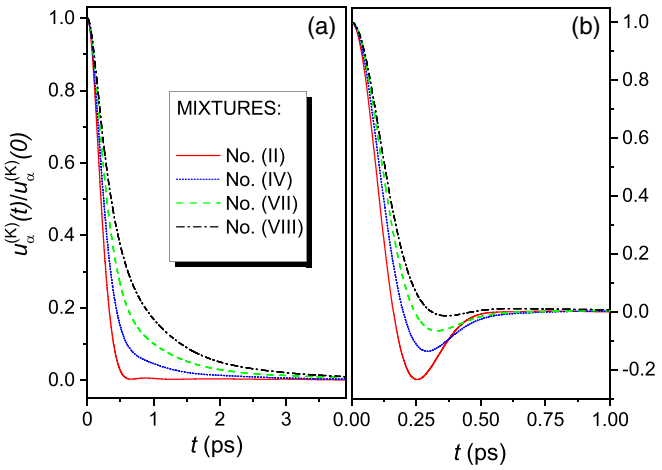

FIG. 2. Selected examples of the canonical velocity autocorrelation functions, $u_\alpha^{(K)}(t)$ (with $\alpha =$ Ne or D_2), obtained from centroid molecular dynamics simulations on four of the samples reported in Table I, namely No. II (red full line), No. IV (blue dotted line), No. VII (green dashed line), and No. VIII (black dot-dashed line). Panel (a) contains the $u_{\rm Ne}^{(K)}(t)/u_{\rm Ne}^{(K)}(0)$ plots and panel (b) the $u_{\rm D_2}^{(K)}(t)/u_{\rm D_2}^{(K)}(0)$ ones. Normalization to 1.0 for $t = 0$ has been introduced for graphic reasons.

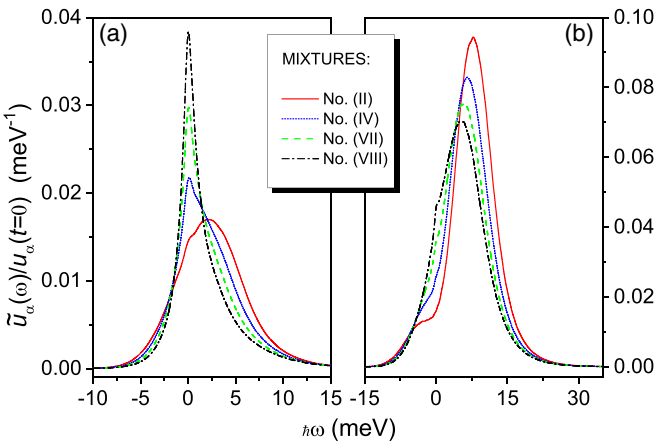

FIG. 3. Selected examples of the spectra of the quantum velocity autocorrelation functions, $\tilde{u}_\alpha(\omega)$ (with $\alpha =$ Ne or D_2), obtained from centroid molecular dynamics simulations on four of the samples reported in Table I, namely No. II (red full line), No. IV (blue dotted line), No. VII (green dashed line), and No. VIII (black dot-dashed line). Panel (a) contains the $\tilde{u}_{\rm Ne}(\omega)/u_{\rm Ne}(t=0)$ plots and panel (b) the $\tilde{u}_{\rm D_2}(\omega)/u_{\rm D_2}(t=0)$ ones. In this way, spectra have been normalized (i.e., their areas are set equal to 1.0) for graphic reasons.

II showing no significant differences with respect to aforementioned CMD calculations with $N = 256$ and $P = 32$ (see Appendix A for details). The three interparticle interactions, namely Ne-Ne, Ne-D_2, and $D_2 - D_2$, have been assumed to be pairwise additive according to the following simple scheme (also used for the mentioned PIMC calculations):

(a) The Ne-Ne interaction was represented by an isotropic Lennard-Jones potential using the parametrization by Morales and Nuevo [36], which has already proved to effectively simulate the Ne-H_2 mixtures [31].

(b) The Ne-D_2 interaction, i.e., that between a D_2 CoM and a Ne atom, was modeled taking the spherical average of the orientation-dependent potential developed by Faubel *et al.* [37], following Challa and Johnson [31] in the case of Ne-H_2 mixtures.

(c) The D_2-D_2 interaction, i.e., that between two molecular D_2 CoMs, was described using the isotropic Silvera–Goldman potential [38].

As mentioned above, in our case the CMD technique produced two physical quantities, $u_\alpha^{(K)}(t)$ with $\alpha =$ Ne or D_2, which approximate the Kubo transforms of the exact quantum VACFs, $u_\alpha(t)$:

$$u_\alpha(t) = \frac{1}{3N_\alpha}\sum_{i=1}^{N_\alpha}\langle \mathbf{v}_i(0)\cdot\mathbf{v}_i(t)\rangle, \tag{3}$$

where $\mathbf{v}_i(t)$ is the velocity of particle i at time t. It is worth recalling that the VACF definition above is slightly different from what can be often found in the literature (e.g., in Ref. [39]), where factor 1/3 is usually absent, but, however, Eq. (3) follows the use of Ref. [40]. Some selected examples of $u_{\rm Ne}^{(K)}(t)$ and $u_{\rm D_2}^{(K)}(t)$ are plotted in Fig. 2, while the corresponding self-diffusion coefficients $D_{\rm Ne}$ and $D_{\rm D_2}$, obtained directly from a time integration (namely, $D_\alpha = \int_0^\infty u_\alpha^{(K)}(t)dt$), are reported in Table I. Since the inversion of Eq. (2) is difficult to handle [41], it is much more convenient to work in the frequency domain of standard Fourier transforms, where the relationship for obtaining the partial VACF spectra $\tilde{u}_\alpha(\omega)$ from the respective canonical counterparts $\tilde{u}_\alpha^{(K)}(\omega)$ is the following [35,41]:

$$\begin{aligned}\tilde{u}_\alpha(\omega) &= \frac{\hbar\omega\beta}{1-\exp(-\hbar\omega\beta)}\tilde{u}_\alpha^{(K)}(\omega)\\ &= \frac{\hbar\omega\beta}{2}\left[\coth\left(\frac{\hbar\omega\beta}{2}\right)+1\right]\tilde{u}_\alpha^{(K)}(\omega).\end{aligned} \tag{4}$$

Examples of $\tilde{u}_{\rm Ne}(\omega)$ and $\tilde{u}_{\rm D_2}(\omega)$ are reported in Fig. 3 for some selected Ne-D_2 mixtures after normalizing their area to unity.

III. DISCUSSION

Once the CMD VACFs had been positively tested against the PIMC simulations as shown in detail in the Appendix B, where we made use of the sum rules reported in Eq. (B1), it was possible to proceed analyzing these functions further to extract the other physical information contained therein. Rigorously speaking, since a thorough theory for the quantum VACFs is still missing, in the rest of the present paper we will focus our attention on the canonical VACFs and their spectra [i.e., $u_\alpha^{(K)}(t)$ and $\tilde{u}_\alpha^{(K)}(\omega)$] rather than their fully quantum counterparts [i.e., $u_\alpha(t)$ and $\tilde{u}_\alpha(\omega)$]. Keeping in mind what has been seen in Appendix B, the reason for such a choice is straightforward since $u_\alpha^{(K)}(t)$ resembles a classical VACF in many respects (for example, it is real-valued and time-symmetric), so that its Fourier spectrum turns out to be real, positive and symmetric in ω. This fact allowed us to carry out a careful analysis of the various canonical VACF estimates exploiting the formalism usually employed in the study of classical liquids, e.g., that based on the so-called Mori-Zwanzig approach [39]. This method, which assumes that any classical time-correlation function is the solution of

a generalized Langevin equation containing a kernel $K_\alpha(t)$, also known as *first-order memory function*, might be applied to our direct CMD outputs, even though we preferred to deal with their Fourier spectra. A rigorous solution of such a generalized Langevin equation can be simply devised in the Laplace space, where a function $f(t)$, originally expressed in the time domain, is represented by $\hat{f}(s)$ in the domain of the conjugate variable, i.e., the complex frequency s, via a Laplace transform: $\hat{f}(s) = \int_0^\infty dt \exp(-st) f(t)$. In addition, due to the ω-symmetry of the Fourier spectrum, $\tilde{f}(\omega)$, one can directly relate it to its Laplace counterpart: $\tilde{f}(\omega) = \pi^{-1} \mathrm{Re}[\hat{f}(i\omega)]$. So, in our case one can write the Langevin equation solution as

$$\hat{u}_\alpha^{(K)}(s) = \frac{u_\alpha^{(K)}(t=0)}{s + \hat{K}_\alpha(s)}. \tag{5}$$

Naturally, the idea behind the Mori-Zwanzig approach is the hypothesis that a memory function is generally simpler than the corresponding time correlation function, so that it is mathematically easier to model the former than the latter, for example, in the framework of a fitting procedure.

A. The Levesque-Verlet model

In our case, we have begun to perform such fits making use of the *Levesque-Verlet* (LV) model [42] for $K_\alpha(t)$, which is quite flexible although still retaining a certain heuristic character:

$$\begin{aligned} K_\alpha(t) &= K_{\alpha,bc}(t) + K_{\alpha,lt}(t) \\ &= \Omega_{E,\alpha}^2 \exp\left(-\frac{B_\alpha}{2} t^2\right) + \frac{L_\alpha}{24} f_\alpha^5 t^4 \exp(-f_\alpha t). \end{aligned} \tag{6}$$

Here the total $K_\alpha(t)$ is written as the sum of two terms: $K_{\alpha,bc}(t)$, the Gaussian part, representing a binary collision term, plus $K_{\alpha,lt}(t)$, the t^4-part, which is meant to describe in an effective way the long-time many-body processes. After performing a Laplace transform on the formula above [42], it reads

$$\begin{aligned} \hat{K}_\alpha(s) &= \hat{K}_{\alpha,bc}(s) + \hat{K}_{\alpha,lt}(s) \\ &= \Omega_{E,\alpha}^2 \sqrt{\frac{\pi}{2B_\alpha}} \exp\left(\frac{s^2}{2B_\alpha}\right) \mathrm{erfc}\left(\frac{s}{\sqrt{2B_\alpha}}\right) + L_\alpha \frac{f_\alpha^5}{(s+f_\alpha)^5}, \end{aligned} \tag{7}$$

which, using Eq. (5), directly provides $\hat{u}_\alpha^{(K)}(s)$ and, subsequently, $\tilde{u}_\alpha^{(K)}(\omega)$ that can be used as a fitting function. The LV model as such contains four free fitting parameters, namely $\Omega_{E,\alpha}$, B_α, L_α, and f_α, which, however, might be reduced to a single parameter (i.e., f_α) by imposing the correct short-time and long-time behaviors of $u_\alpha^{(K)}(t)$. The first and the second parameters may be obtained via a Taylor expansion [42] extending a relationship already used in Eq. (B1):

$$\frac{u_\alpha^{(K)}(t)}{u_\alpha^{(K)}(0)} = 1 - \frac{1}{2}\Omega_{E,\alpha}^2 t^2 + \frac{1}{24}\Omega_{E,\alpha}^2(\Omega_{E,\alpha}^2 + B_\alpha) t^4 + \cdots; \tag{8}$$

the third by exploiting the definition of D_α in terms of $\hat{u}_\alpha^{(K)}(s)$ and $\hat{K}_\alpha(s)$:

$$\begin{aligned} D_\alpha &= \hat{u}_\alpha^{(K)}(s=0) = \frac{u_\alpha^{(K)}(t=0)}{\hat{K}_\alpha(s=0)} \\ &= M_\alpha^{-1} k_B T \left(\Omega_{E,\alpha}^2 \sqrt{\frac{\pi}{2B_\alpha}} + L_\alpha\right)^{-1}. \end{aligned} \tag{9}$$

However, during the actual LV fitting procedure, we have decided to make use of all the four free parameters, since a single-parameter fit would have been too rigid. Final results for the LV fits are plotted in Fig. 4 for some selected spectra of both species, while all the numerical values for $\Omega_{E,\alpha} B_\alpha$ (squared binary collision frequency), L_α (long-time memory function intensity), and f_α (long-time frequency) are reported in Table II.

The agreement between CMD simulations and LV fits is generally very good for both species at all concentration/density values investigated, even though a zoom on the low-ω range (say, ± 1 ps^{-1}) would show some small discrepancies which have a limited impact on the D_α estimates produced by the fit, as shown in Fig. 5. Such a low-ω range is connected with the long-t tail of $u_\alpha^{(K)}(t)$ which might be not perfectly fitted by the LV model, even though one should also note that our CMD correlation functions were calculated up to a maximum time lag of 5.00 ps, an interval which implies a minimum ω binning of 0.628 ps^{-1}. This means that only two or three data points in the -1 ps$^{-1} < \omega < 1$ ps^{-1} range are really significant. The $\Omega_{E,\alpha}$ values obtained from the LV fits (see Table II) compare quite satisfactorily with the original CMD values reported in Fig. 6, although the former slightly underestimate the latter, especially in the D_2 case at high n values. Unsurprisingly, as we have already seen before, this physical quantity exhibits a strong increase along with the system density, quite differently to what B_α actually does. In fact, Fig. 7 clearly shows that the estimates of the latter increase as the D_2 concentration grows (and n decreases) for both molecular species. However, one can also observe a shift (almost rigid) between the B_α data sets derived directly from the CMD VACFs via Eq. (8) on one side, and the LV fit outputs in Table II on the other: the LV fitting procedure generally tends to underestimate this physical quantity, so that the comparison between the two approaches is less satisfactory here than in the $\Omega_{E,\alpha}$ case. In addition, it is worthwhile to note that looking at the aforementioned equation, one can finally give a precise meaning to B_α: if $\tilde{u}_\alpha^{(K)}(\omega)/u_\alpha^{(K)}(t=0)$ is interpreted as a symmetric probability density distribution, then $\Omega_{E,\alpha}^2$ represents the variance of such a distribution and B_α is simply related to the corresponding coefficient of kurtosis [43] γ_α: $B_\alpha = \Omega_{E,\alpha}^2(\gamma_\alpha + 2)$.

However, the trends of the other two fitting parameters, L_α and f_α, are less simple to be interpreted: while L_{D_2} seems to decrease as n grows, its Ne counterpart does not show a clear tendency and remains more or less constant. Similarly, the two f_α sets do not exhibit a definite trend as a function of the concentration/density. However, what is slightly unexpected is the sign change of L_{D_2} when n decreases, and the fact that L_{Ne} is always negative except for sample No. I. As a matter of fact, if $L_\alpha < 0$ then one obtains that also $K_{\alpha,lt}(t) < 0$ for all t values, while $K_\alpha(t)$ becomes negative for t larger than a

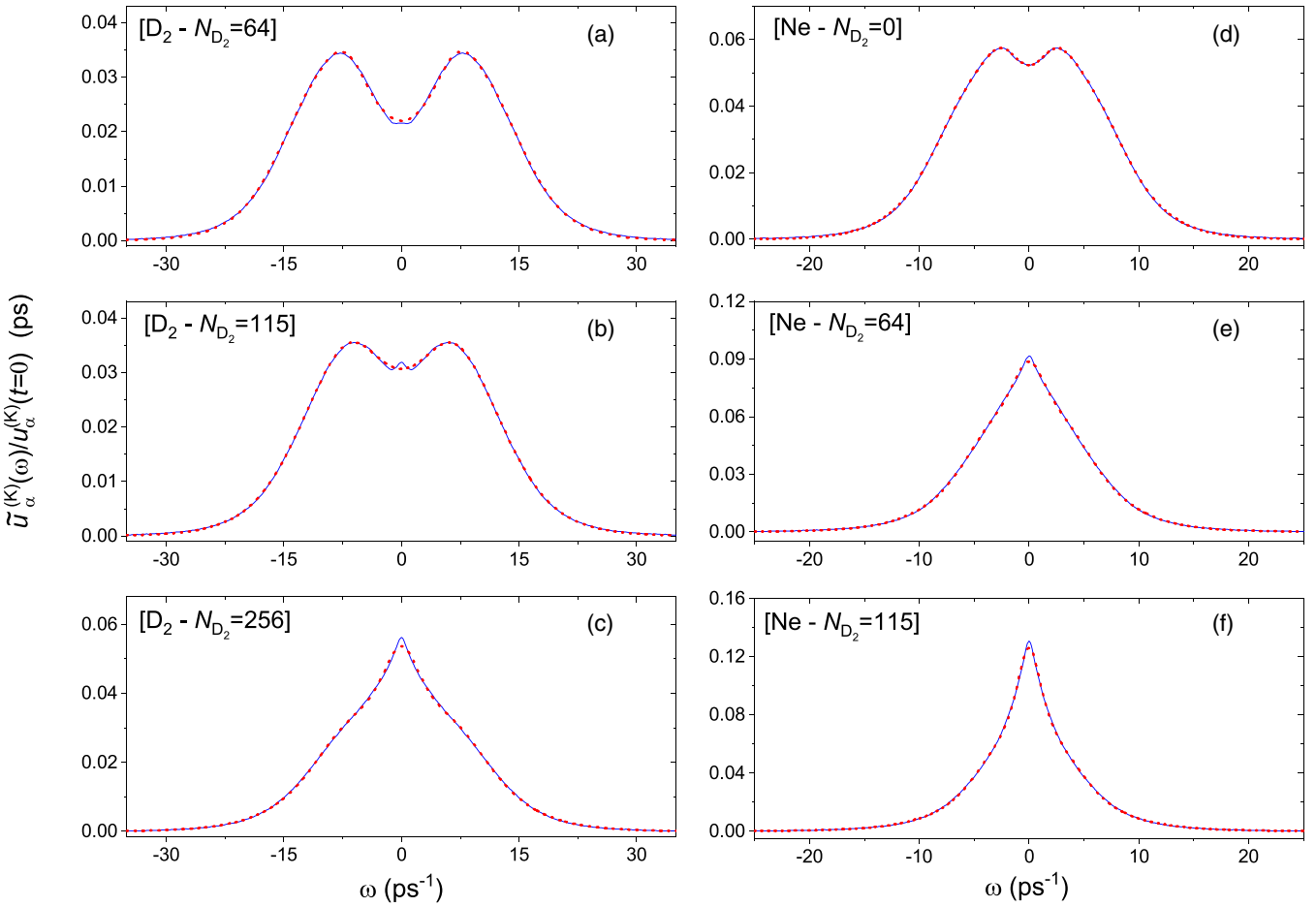

FIG. 4. Selected examples of the canonical VACF spectra, $\tilde{u}_{\alpha}^{(K)}(\omega)$ (with α = Ne or D_2), obtained from CMD simulations (blue full lines), together with their best fits using the LV memory function approach (red dotted lines). Four concentrations have been selected from those reported in Table I, namely No. I [panel (d)], No. III [panels (a) and (e)], No. V [panels (b) and (f)], and No. X [panel (c)]. Panels (a), (b), and (c) contain the $\tilde{u}_{D_2}^{(K)}(\omega)/u_{D_2}^{(K)}(t=0)$ plots and panels (d), (e), and (f) the $\tilde{u}_{Ne}^{(K)}(\omega)/u_{Ne}^{(K)}(t=0)$ ones. In this way spectra have been normalized (i.e., their areas are set equal to 1.0) for graphic reasons.

certain time threshold. Unfortunately, the LV model, due to its heuristic nature, does not allow to shed more light on the physical meaning of these findings concerning $K_{\alpha,lt}(t)$, and so we had to resort to another memory function model.

B. The itinerant oscillator model

As mentioned in the introductory section, a historically relevant approach to the classical VACF analysis is

TABLE II. Results of the fitting procedure of the canonical VACF spectra from CMD using the LV memory function, including: simulation number "No.," deuterium concentration x_{D_2}, total molecular density n, Ne and D_2 Einstein frequencies ($\Omega_{E,Ne}$ and Ω_{E,D_2}), Ne and D_2 squared binary collision frequencies (B_{Ne} and B_{D_2}), Ne and D_2 long-time memory function intensities (L_{Ne} and L_{D_2}), Ne and D_2 long-time frequencies (f_{Ne} and f_{D_2}). Statistical errors are reported in parentheses.

No.	x_{D_2} (%)	n (nm^{-3})	$\hbar\Omega_{E,Ne}$ (meV)	$\hbar\Omega_{E,D_2}$ (meV)	B_{Ne} (ps^{-2})	B_{D_2} (ps^{-2})	L_{Ne} (ps^{-1})	L_{D_2} (ps^{-1})	f_{Ne} (ps^{-1})	f_{D_2} (ps^{-1})
I	0.00	34.44	4.260(3)	—	86.1(3)	—	0.431(7)	—	5.99(6)	—
II	14.84	30.71	3.885(7)	7.723(9)	94.3(8)	162(1)	−0.109(8)	4.30(5)	7.9(5)	13.79(9)
III	25.00	28.60	3.70(1)	7.255(7)	104(1)	167.5(8)	−0.302(9)	2.72(3)	6.6(2)	13.47(8)
IV	35.16	26.80	3.54(1)	6.927(5)	115(2)	174.3(6)	−0.409(9)	1.71(1)	6.6(1)	13.62(8)
V	44.92	25.34	3.42(2)	6.655(5)	128(3)	182.6(8)	−0.457(9)	0.92(1)	6.7(1)	14.4(1)
VI	50.00	24.67	3.36(2)	6.531(6)	136(3)	186.6(9)	−0.453(9)	0.63(1)	6.6(1)	15.0(2)
VII	55.08	24.07	3.31(2)	6.436(9)	147(4)	190(1)	−0.453(9)	0.40(2)	6.6(1)	16.0(6)
VIII	75.00	22.33	3.16(3)	6.132(8)	201(8)	206(1)	−0.373(7)	−0.45(1)	7.0(1)	8.0(2)
IX	85.16	21.80	3.11(3)	6.02(1)	227(9)	213(2)	−0.344(6)	−0.59(1)	7.3(1)	9.8(2)
X	100.00	21.41	—	5.94(1)	—	226(2)	—	−0.87(1)	—	12.1(2)

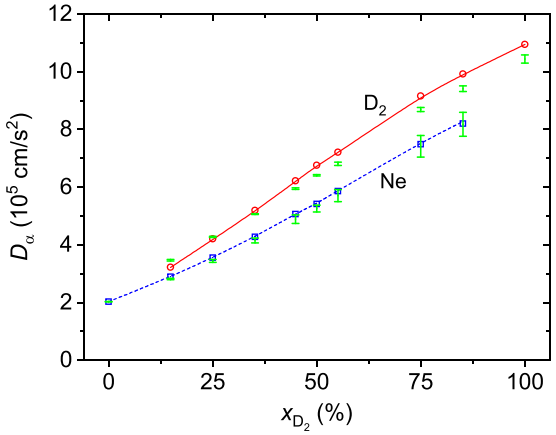

FIG. 5. Self-diffusion coefficients D_α (with α = Ne or D_2) as a function of x_{D_2} obtained from CMD simulations. Blue symbols and blue dashed line stand for Ne, while red symbols and red full line for the D_2 center of mass. Empty symbols refer to the raw values reported in Table I, while lines are splines through the data corrected according to the procedure described in the text to cope with the small effects discussed in Appendix B and shown in Fig. 13. Green error bars represent the D_α estimates from the Levesque-Verlet fitting procedure of the CMD VACF data. Statistical errors smaller than the symbol size are not reported.

represented by the various IO models [16], where a single particle rattles inside pseudocages (made of neighbor molecules) with a frequency ω_0, a time-dependent friction coefficient $\mu(t)$, and a mass M_0, while these pseudocages move in the bulk liquid with a frequency ω_1, a time-dependent friction coefficient $\nu(t)$, and a mass M_1. Such a scenario seems particularly suitable for the study of the self-dynamics of D_2 molecules in a neon-rich liquid mixture, since the light-

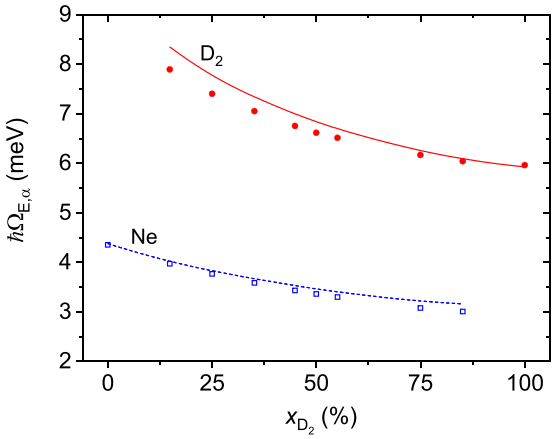

FIG. 6. Einstein frequency values $\hbar\Omega_{E,\alpha}$ (with α = Ne or D_2) as a function of x_{D_2} obtained from CMD simulations compared with the corresponding results derived from potential Laplacians and SPCFs via Eq. (B5) as explained in Appendix B. Blue color stands for Ne, while red color stands for the D_2 center of mass. Lines (dashed for Ne and full for D_2) are splines through the PIMC/SPCF-based data, while symbols (empty squares for Ne and full circles for D_2) refer to CMD estimates, whose statistical errors are smaller than the symbol size.

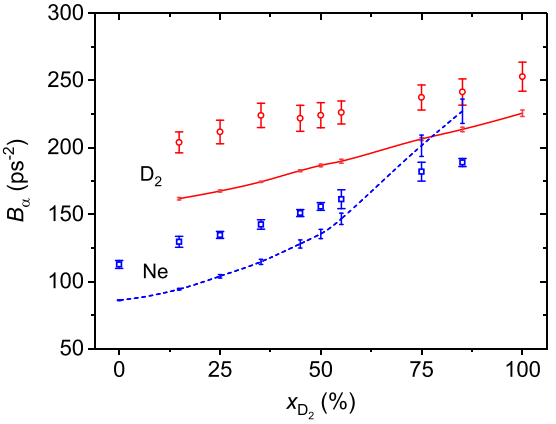

FIG. 7. Coefficients B_α (with α = Ne or D_2) as a function of x_{D_2} obtained either directly from the CMD simulations or, indirectly, via their LV fits. Blue squares and blue dashed line stand for Ne, while red circles and red full line stand for the D_2 center of mass. Empty symbols refer to the short-time expansion in Eq. (8) applied to the CMD outputs, while lines are splines obtained from the Levesque-Verlet fitting procedure operated on the spectra of the same CMD data. Statistical uncertainties are plotted as error bars.

molecule rattling dynamics might appear to be well decoupled from the pseudocage motion, due to the large mass difference between these two entities. The twofold IO dynamics can be modelled by two coupled Langevin equations [44], including the particle coordinates as well as the position of the pseudocage centroid and giving rise to a manageable formula for the Laplace transform of the memory function, $\hat{K}_{IO}(s)$:

$$\hat{K}_{IO}(s) = \hat{\mu}(s) + \frac{\omega_0^2[s+\hat{\nu}(s)]}{s[s+\hat{\nu}(s)]+\omega_1^2}. \tag{10}$$

However, this IO formula does not specify the time dependence of the two friction coefficients $\mu(t)$ and $\nu(t)$. In what follows we have assumed the former to be strictly Gaussian: $\mu(t) = a_0\tau_0^{-1}\exp[-\frac{\pi}{4}(t/\tau_0)^2]$, corresponding to a Laplace transform: $\hat{\mu}(s) = a_0\exp(s^2\tau_0^2/\pi)\mathrm{erfc}(s\tau_0/\sqrt{\pi})$; while for the latter, following Ref. [44], the exponential option has been implemented: $\nu(t) = a_1\tau_1^{-1}\exp(-|t|/\tau_1)$, with: $\hat{\nu}(s) = a_1/(1+s\tau_1)$. In this way, exploiting Eq. (5), it was possible to set up a fitting model including six free parameters. Namely, three for the particle rattling: ω_0, a_0, τ_0, and three for the pseudocage motion: ω_1, a_1, τ_1. Of course, it is possible to combine the six parameters above to recover the three physical quantities we have dealt with earlier, i.e., Ω_E, D and B (where the suffix "α" has been dropped here for the sake of simplicity):

$$\begin{aligned}
\Omega_E^2 &= \lim_{s\to+\infty} s\hat{K}_{IO}(s) = a_0\tau_0^{-1} + \omega_0^2,\\
D &= \frac{u^{(K)}(t=0)}{\hat{K}_{IO}(0)} = \frac{k_BTM^{-1}}{a_0 + a_1\omega_0^2\omega_1^{-2}},\\
B &= -\frac{1}{2\Omega_E^2}\lim_{s\to+\infty}\left[s^3\hat{K}_{IO}(s) - s^2\Omega_E^2\right]\\
&= \frac{\omega_0^2\omega_1^2}{\Omega_E^2} + \frac{a_0\pi}{2\tau_0^3\Omega_E^2}.
\end{aligned} \tag{11}$$

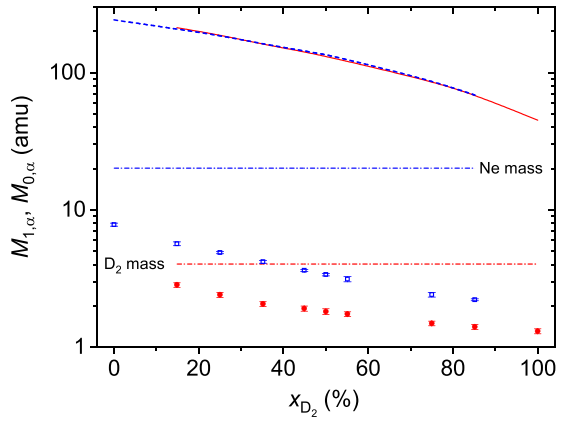

FIG. 8. Mass parameters $M_{1,\alpha}$ (with $\alpha = \text{Ne or } D_2$), representing the effective masses of the pseudocages in the CE model, are reported as symbols with error bars as a function of x_{D_2}. Full and dashed lines mark the $M_{1,\alpha}$ values obtained from the SPCFs, while dot-dashed horizonal lines stand for the corresponding $M_{0,\alpha}$ values, i.e., the masses of the rattling particles. Red full circles and red full line represent D_2, while blue empty squares and blue dashed line are for Ne.

Coffrey and Evans [45] devised a simplified version of the IO model (labeled CE in what follows) where the friction coefficient for the particle rattling is completely neglected [i.e., $\mu(t) = 0$], while that for the pseudocage motion is taken as impulsive [$\nu(t) = \beta\delta(t)$]. These assumptions give rise to a three-parameter memory function:

$$\hat{K}_{CE}(s) = \frac{\omega_0^2(s+\beta)}{s(s+\beta)+\omega_1^2}, \tag{12}$$

where it is possible to prove that

$$\begin{aligned} \Omega_E^2 &= \omega_0^2, \\ B &= \omega_1^2, \\ D &= \frac{k_B T \omega_1^2}{M\beta\omega_0^2}. \end{aligned} \tag{13}$$

Since in both IO and CE the fundamental assumption [44] is that $\omega_0^2/\omega_1^2 = M_1/M_0$, and M_0 is known, it is possible to exploit CE (for both species α) to roughly estimate the average pseudocage mass $M_{1,\alpha}$ directly from the B_α data reported in Fig. 7: $M_{1,\alpha} \approx M_{0,\alpha}(\Omega_{E,\alpha}^2/B_\alpha)$. For the sake of clarity, it is worth recalling that the symbol $M_{0,\alpha}$ stands for the mass of a rattling particle belonging to the species α, while the symbol $M_{1,\alpha}$ represents the average mass of a pseudocage surrounding a particle belonging to the species α (such a pseudocage being made in general by particles of both species in numbers depending on x_{D_2}). The results, shown in Fig. 8, are quite surprising since $M_{1,\alpha}$, belonging to the pseudocage as a whole, turns out to to be consistently smaller than $M_{0,\alpha}$ which pertains to the rattling particle trapped inside it. On the contrary, making use of the partial static pair correlation functions, $g_{\alpha,\alpha}(r)$ and $g_{\alpha,\beta}(r)$, from PIMC, one can simply estimate $M_{1,\alpha}$ from the following formula:

$$M_{1,\alpha} = 4\pi n\left(M_{0,\alpha}\, x_\alpha \int_0^{R_{\alpha,\alpha}} r^2 g_{\alpha,\alpha}(r)dr + M_{0,\beta}\, x_\beta \int_0^{R_{\alpha,\beta}} r^2 g_{\alpha,\beta}(r)dr\right), \tag{14}$$

where $R_{\alpha,\alpha}$ and $R_{\alpha,\beta}$ represent the limits of the nearest neighbor shell in $g_{\alpha,\alpha}(r)$ and $g_{\alpha,\beta}(r)$, respectively, i.e., their first minima. Results are plotted in Fig. 8 where the large differences from the mentioned CE estimates are clearly evident. As a matter of fact, the partial SPCF analysis shows that the pseudocages are formed by $\mathcal{N}_\alpha(n)$ nearest neighbor molecules, with $10.4 < \mathcal{N}_\alpha(n) < 12.7$. In addition, it turns out that $\mathcal{N}_\alpha(n)$ is almost independent of the species α of the central particle [i.e., $\mathcal{N}_\alpha(n) \approx \mathcal{N}(n)$], while it is only mildly increasing with the total molecular density n. So it is expected that $M_{1,\alpha} \approx \mathcal{N}(n)(M_{0,\alpha}\, x_\alpha + M_{0,\beta}\, x_\beta)$. This noticeable discrepancy between CE-based and PIMC-based estimates might be interpreted as the effect of an error in the CMD output analysis, but actually this is not the case since a similar situation was already noticed in Ref. [44] concerning the VACF of liquid Ar at $T = 94.4$ K and $n = 20.712\ \text{nm}^{-3}$. In this case ω_0 and ω_1 were evaluated using the full IO model reported above and provided a rather peculiar result: $(\omega_0/\omega_1)^2 = 1.5/2.1 \approx 0.71$. As we have seen earlier, in the IO framework this finding implies that $M_1 \approx 0.71\, M_0$. Now, assuming for liquid Ar in the mentioned conditions an $\mathcal{N} = 12.53$ [46], from the SPCF analysis one would expect $M_1 = 12.53\, M_0$ instead of $M_1 \approx 0.71\, M_0$. This result should be compared with our pure Ne calculation on sample No. I, where one obtains $M_1 = 0.39\, M_0$, instead of $M_1 = 12.05\, M_0$.

Since the issue of the pseudocage mass is quite relevant, and the CE model offers only a coarse description of the CMD data, it was decided to perform an accurate IO fitting of all the $\tilde{u}_\alpha^{(K)}(\omega)$ spectra using the memory function of Eq. (10). However, differently from the LV fitting procedure, we have used the first and the last constraints in Eq. (11) to reduce the number of free parameters to four: ω_0, τ_0, τ_1, and $\hat{K}_{IO}^{-1}(0)$. Moreover, we found that the fit did not exhibit a strong dependence on τ_1 whenever this parameter became lower than (or comparable to) τ_0. So we decided to keep τ_1 fixed to 0 (actually, to $1.00 \cdot 10^{-9}$ ps for numerical reasons) arriving at a three-parameter IO fitting procedure. This assumption implied that the time-dependent friction coefficient $\nu(t)$ could be safely approximated by a Dirac δ function. Final results for the IO fits are plotted in Fig. 9 for some selected spectra of both species, while the corresponding numerical values for the physically most relevant IO parameters (i.e., ω_0, ω_1, and τ_0) are reported in Table III together with the new estimates of $M_{1,\alpha}$. These values, comparing Table III with Fig. 8, turned out to be even lower than the corresponding CE results, leaving the problem of the large discrepancy between the structural and dynamical $M_{1,\alpha}$ estimates still unsolved. We will try to address this issue in the concluding section.

As for the quality of the IO fitting procedure, which is globally good as shown in Fig. 9, we have to note that it deteriorates as n decreases (i.e., x_{D_2} grows) for both species. In particular, for samples Nos. VII–X, the statistical uncertainties

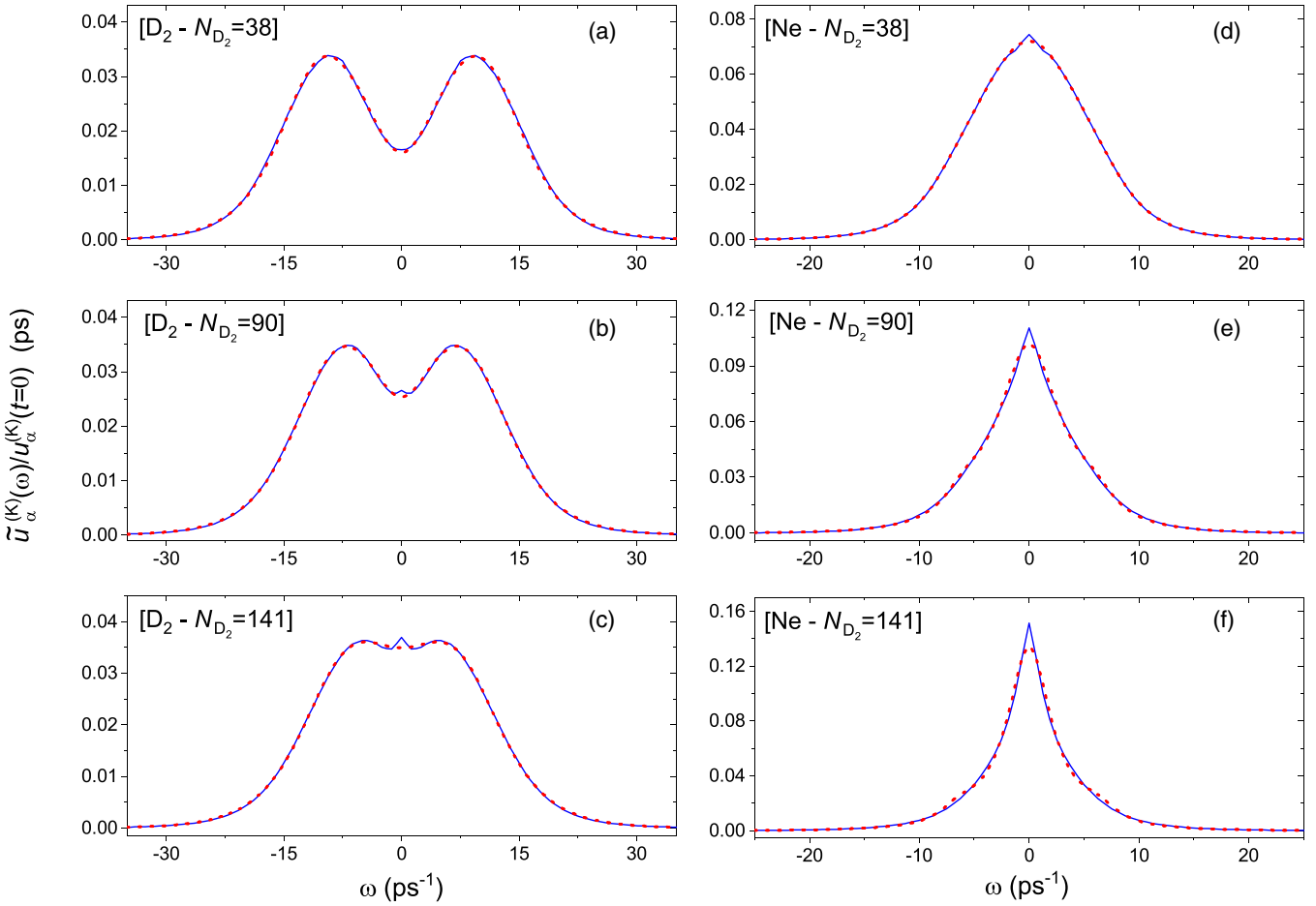

FIG. 9. Selected examples of the canonical VACF spectra, $\tilde{u}_\alpha^{(K)}(\omega)$ (with α = Ne or D_2), obtained from CMD simulations (blue full lines), together with their best fits using the IO memory function approach of Eq. (10) (red dotted lines). Three concentrations have been included among those reported in Table I, namely No. II [panels (a) and (d)], No. IV [panels (b) and (e)], and No. VII [panels (c) and (f)]. Panels (a), (b), and (c) contain the $\tilde{u}_{D_2}^{(K)}(\omega)/u_{D_2}^{(K)}(t=0)$ plots and panels (d), (e), and (f) the $\tilde{u}_{Ne}^{(K)}(\omega)/u_{Ne}^{(K)}(t=0)$ ones. In this way, spectra have been normalized (i.e., their areas are set equal to 1.0) for graphic reasons.

on the ω_0 estimates become substantially larger. If compared to the LV fits (which, however, include four free parameters), the three-parameter IO fits are always worse for Ne, except in case of samples Nos. I and II, where the respective reduced chi-squared (χ_r^2) values are roughly similar. On the contrary, moving to D_2 the situation with χ_r^2 is somehow different: IO is superior to LV at high density up to sample No. II, becoming comparable for samples Nos. III–VII, and then ending as

TABLE III. Results of the fitting procedure of the canonical VACF spectra from CMD operated using the IO memory function of Eq. (10), including: simulation number "No.," deuterium concentration x_{D_2}, molecular rattling frequency for the α species $\omega_{0,\alpha}$, corresponding friction coefficient (Gaussian) time constant, $\tau_{0,\alpha}$, pseudocage frequency $\omega_{1,\alpha}$, and estimated pseudocage mass $M_{1,\alpha}$. Statistical errors are reported in parentheses.

No.	x_{D_2} (%)	$\omega_{0,Ne}$ (ps^{-1})	ω_{0,D_2} (ps^{-1})	$\tau_{0,Ne}$ (ps)	τ_{0,D_2} (ps)	$\omega_{1,Ne}$ (ps^{-1})	ω_{1,D_2} (ps^{-1})	$M_{1,Ne}$ (a.m.u.)	M_{1,D_2} (a.m.u.)
I	0.00	4.65(4)	—	0.1091(4)	—	9.65(5)	—	4.68(9)	—
II	14.84	3.84(4)	5.19(2)	0.1031(6)	0.0840(2)	10.1(2)	11.0(2)	2.9(1)	0.89(3)
III	25.00	2.9(1)	4.31(2)	0.0988(5)	0.0853(1)	7.7(2)	13.6(1)	2.9(2)	0.404(9)
IV	35.16	2.18(7)	3.73(3)	0.0984(5)	0.0859(1)	6.4(1)	17.4(2)	2.4(2)	0.185(4)
V	44.92	2.00(6)	3.20(5)	0.0959(4)	0.0862(2)	6.1(2)	17.8(3)	2.2(2)	0.130(6)
VI	50.00	2.04(7)	3.03(7)	0.0939(5)	0.0863(2)	6.2(2)	18.9(4)	2.2(2)	0.103(8)
VII	55.08	2.2(1)	3.0(2)	0.0910(9)	0.0865(3)	6.7(2)	19.6(8)	2.2(3)	0.09(1)
VIII	75.00	3.7(5)	4.7(1)	0.072(7)	0.0776(3)	10.2(8)	13.0(4)	2.6(8)	0.53(4)
IX	85.16	3.9(5)	4.8(2)	0.06(1)	0.0758(2)	11(1)	12.4(4)	2.6(8)	0.60(6)
X	100.00	—	4.3(2)	—	0.0738(4)	—	11.4(3)	—	0.57(7)

clearly inferior for the lowest density mixtures and the pure D_2 liquid. This behavior is not completely unexpected and, leaving aside the problem of the fitted M_1 values for the moment, points to the fact that the IO model seems more justified when the rattling mass is low (e.g., D_2) and the pseudocage mass is large (e.g., low x_{D_2} corresponding to high n). Finally, another IO fitting scheme was devised to rule out even the most remote possibility that the fitted ratios $M_{0,\alpha}/M_{1,\alpha}$ were somehow conditioned by our model-parametrization choice. The two canonical VACF spectra best described by the IO model were selected, namely those for D_2 belonging to samples Nos. II and III, and refitted using a full six-parameter function (i.e., ω_0, a_0, τ_0, ω_1, a_1, and τ_1) plus a linear constraint: $\omega_{1,D_2} = (2M_D/M_{1,D_2})^{1/2}\omega_{0,D_2}$, forcing in this way the pseudocage frequency to exhibit the correct behavior according to the pseudocage mass estimated via the PIMC SPCFs. In particular, M_{1,D_2} was taken as 212.874 and 188.501 amu for samples Nos. II and III, respectively. This corresponded to $(\omega_{0,D_2}/\omega_{1,D_2})$ equal to 7.271 (for No. II) and 6.842 (for No. III). Fitting results turned out to be extremely poor for both samples, especially in the low ω range, where it was evident that the CMD data fit required $(\omega_{0,D_2}/\omega_{1,D_2}) < 1$.

C. The exponential expansion theory approach

Given this peculiar and puzzling situation, we decided to try interpreting the $u_\alpha^{(K)}(t)$ data from CMD via a new approach known as *exponential expansion theory* (EET), which has been successfully applied to the study of the VACF of various systems ranging from fluid para-H_2 [47,48] to liquid Au [49] and the classical Lennard-Jones liquids [50,51]. This theoretical framework is actually very general and perfectly suits all the real, time-symmetric autocorrelation functions, including the Kubo-transformed ones when quantum effects play a relevant role [52]. From a practical point of view, for $t \geqslant 0$, the correlation function is always represented by a finite sum of exponentials (modes):

$$u_\alpha^{(K)}(t) = u_\alpha^{(K)}(0)\sum_{j=1}^{N_m}[I_j \exp(z_j t) + I_j^* \exp(z_j^* t)], \qquad (15)$$

where the I_j and z_j parameters are generally complex numbers to be determined under the condition that $\mathrm{Re}[z_j] \leqslant 0$ for each mode, with j ranging from 1 to N_m, the total number of modes required. This number is not determined *a priori*, since N_m is strongly influenced by the thermodynamic state of the sample and by the accuracy of the data and the fitting procedure, but it is typically lower than 10. The complex frequencies z_j contain two parts, i.e., $\mathrm{Re}[z_j]$ and $\mathrm{Im}[z_j]$, with the former part (i.e., $\mathrm{Re}[z_j]$) representing the mode damping Γ_j and the latter part (i.e., $\mathrm{Im}[z_j]$) the mode angular frequency ω_j, although purely dissipative modes with $\omega_j = 0$ can also be present (e.g., representing thermal diffusion decay processes). In other words, $z_j = -\Gamma_j + i\omega_j$ (and $z_j^* = -\Gamma_j - i\omega_j$). Thus, for $t \geqslant 0$, Eq. (15) can always be cast in a slightly different form:

$$u_\alpha^{(K)}(t) = 2u_\alpha^{(K)}(0)\sum_{j=1}^{N_m}|I_j|\exp(-\Gamma_j t)\cos(\omega_j t + \phi_j), \qquad (16)$$

where $I_j = |I_j|\exp(i\phi_j)$ with $|I_j|$ representing the amplitude of the j^{th} mode. This implies that the exponential expansion in the Laplace space reads

$$\frac{\hat{u}_\alpha^{(K)}(s)}{u_\alpha^{(K)}(t=0)} = 2\sum_{j=1}^{N_m}|I_j|\frac{(\Gamma_j + s)\cos\phi_j - \omega_j \sin\phi_j}{(\Gamma_j + s)^2 + \omega_j^2}, \qquad (17)$$

which in the Fourier space corresponds to

$$\frac{\tilde{u}_\alpha^{(K)}(\omega)}{u_\alpha^{(K)}(t=0)} = \sum_{j=1}^{N_m}|I_j|\left[\frac{\Gamma_j\cos\phi_j - (\omega+\omega_j)\sin\phi_j}{\Gamma_j^2 + (\omega+\omega_j)^2} + \frac{\Gamma_j\cos\phi_j - (\omega-\omega_j)\sin\phi_j}{\Gamma_j^2 + (\omega-\omega_j)^2}\right]. \qquad (18)$$

In addition, some sum rules can be imposed to comply with some exact physical constraints. In particular, the zeroth sum rule is simply obtained by evaluating Eq. (15) for $t = 0$, that is $\sum_{j=1}^{N_m}(I_j + I_j^*) = 1$, while the higher-order sum rules can be worked out keeping in mind that the odd derivatives of $u_\alpha^{(K)}(t)$ evaluated at $t = 0^+$ are equal to zero, as already seen in Eq. (8). For example, the first sum rule can be simply written as $\sum_{j=1}^{N_m}(z_j I_j + z_j^* I_j^*) = 0$.

While fitting the D_2 canonical VACFs we have always made use of three complex pairs (3C, involving three frequencies, ω_{1-3}, and three damping coefficients, Γ_{1-3}), except for the samples at the lowest densities values, namely, Nos. VIII, IX, and X, where two complex pairs (2C) and two real dissipative (2R) modes (i.e., two frequencies. $\omega_{1,2}$, and four damping coefficients, Γ_{1-4}) have been utilized. It is important to stress that when three complex pairs are included, only the first two have to be considered as physically meaningful since the third, which is characterized by large values of both ω_3 and Γ_3 but a very low value of $|I_3|$, is needed only to improve the fit quality accounting, for example, for small computational inaccuracies. Similarly, for samples Nos. VIII, IX, and X where two complex pairs are used, only one is considered relevant. Various reasons can be given to justify this choice: for example, $\hbar\omega_3$ turns out to be unphysically larger than $k_B\Theta_{D,D_2}$ (see Table I), where the latter quantity approximately marks the upper limit of the collective excitation energies involving the D_2 molecules of the system. In addition, it is worth mentioning the fact that in quite a different context (i.e., a set of slightly supercritical monatomic Lennard-Jones fluids [50]) similar high-frequency modes showed up in the analysis of the VACFs of these systems. For this reason, only $|I_{1,2}|$, $\phi_{1,2}$, $\Gamma_{1,2}$, and $\omega_{1,2}$ are reported in Table IV.

As for the Ne canonical VACFs, the EET fitting procedure was similar to that used in the D_2 case, even though the distribution of complex and real modes was not identical: for samples Nos. II–VII two complex pairs (2C) and one real dissipative (1R) mode (i.e., two frequencies and three damping coefficients) have been employed. All these three modes were considered as physically meaningful despite the fact that the second was characterized by a rather low value of $|I_2|$. Sample No. I, i.e., pure Ne, needed an additional dissipative mode, including two complex pairs (2C) and two real (2R) modes (i.e., two frequencies and four damping coefficients). However, in this case, similarly to what we have seen above, the 2nd C mode was regarded as unphysical, due to its high

TABLE IV. Selected results of the EET fitting procedure of the canonical VACFs for the α (= Ne or D_2) species. Table includes: simulation number "No.," deuterium concentration x_{D_2}, applied fitting scheme, mode number of the propagating excitations (C), their frequencies ω_α, damping coefficients Γ_α, amplitudes $|I_\alpha|$, and phases ϕ_α. Available statistical errors are reported in parentheses. Only propagating modes with a relevant amplitude are reported, while diffusive modes (R) have been always omitted.

No.	x_{D_2} (%)	Fit scheme Ne	D_2	Mode	ω_{Ne} (ps^{-1})	ω_{D_2} (ps^{-1})	Γ_{Ne} (ps^{-1})	Γ_{D_2} (ps^{-1})	$\lvert I_{Ne}\rvert$	$\lvert I_{D_2}\rvert$	ϕ_{Ne} (rad)	ϕ_{D_2} (rad)
I	0.00	2C+2R	—	1st C	8.10(4)	—	6.00(3)	—	0.479	—	−1.374	—
				2nd C	—	—	—	—	—	—	—	—
II	14.84	2C+1R	3C	1st C	6.74(5)	6.30(7)	5.88(1)	7.5(3)	0.430	0.671	−1.279	0.860
				2nd C	19.2(3)	15.2(1)	14.8(6)	8.7(2)	0.012	0.476	−3.499	−1.441
III	25.00	2C+1R	3C	1st C	5.34(6)	5.2(2)	5.58(7)	7.6(3)	0.533	0.707	−0.932	0.868
				2nd C	16.9(3)	14.19(7)	16.2(7)	9.0(2)	0.019	0.483	−3.820	−1.480
IV	35.16	2C+1R	3C	1st C	4.5(1)	5.1(2)	5.7(1)	7.6(2)	0.605	0.683	−0.961	0.740
				2nd C	17.3(3)	13.68(8)	16(1)	9.3(2)	0.018	0.457	−3.687	−1.578
V	44.92	2C+1R	3C	1st C	3.94(6)	5.4(5)	5.74(9)	7.8(4)	0.612	0.641	−0.997	0.528
				2nd C	18.0(2)	13.3(3)	14.6(9)	9.6(4)	0.016	0.427	−3.342	−1.693
VI	50.00	2C+1R	3C	1st C	3.63(9)	5.9(6)	5.7(1)	8.2(5)	0.618	0.651	−1.019	0.330
				2nd C	18.2(3)	13.3(6)	13.5(8)	10.1(5)	0.016	0.410	−3.127	−1.855
VII	55.08	2C+1R	3C	1st C	3.1(1)	5.6(6)	6.0(1)	9.0(4)	0.708	0.677	−1.103	0.386
				2nd C	18.4(2)	12.6(5)	14.3(8)	10.2(2)	0.015	0.482	−3.207	−1.835
VIII	75.00	1C+2R	2C+2R	1st C	7.5(4)	—	14.9(4)	—	0.129	—	−3.278	—
				2nd C	—	10.68(4)	—	9.93(6)	—	0.682	—	−1.429
IX	85.16	1C+2R	2C+2R	1st C	10(1)	—	13(2)	—	0.088	—	−2.819	—
				2nd C	—	10.9(1)	—	10.0(2)	—	0.582	—	−1.531
X	100.00	—	2C+2R	1st C	—	—	—	—	—	—	—	—
				2nd C	—	11.05(5)	—	9.63(4)	—	0.505	—	−1.459

value of ω_2 and its tiny value of $|I_2|$. Moving to samples Nos. VIII and IX, the mode selection changed again: one complex pair (1C) and two real dissipative (2R) modes (i.e., one frequency and three damping coefficients) were used in the EET fits. Also this time all the three modes were taken as relevant and, moreover, none of their amplitudes, $|I_{1,2,3}|$, was much smaller than the other two. Given this scenario, in the case of Ne, the main propagating mode parameters, $|I_1|$, ϕ_1, Γ_1, and ω_1, are reported in Table IV for all the samples, while those related to the 2nd C mode, i.e., $|I_2|$, ϕ_2, Γ_2, and ω_2, appear only for samples Nos. II–VII. At this stage it is worthwhile to point out that the mode type selection was not arbitrary at all, but it was always driven by both physical reasons and fit quality. For instance, in the D_2 case the EET fit with three complex pairs (3C) was really excellent for sample No. II, remaining substantially very good up to sample No. VII. Then, after reaching sample No. VIII, the mode selection was changed, moving to two complex pairs (2C) and two real dissipative modes (2R), and the fit result was excellent again for all the remaining samples. Selected examples of the EET fits for Ne and D_2 canonical VACFs can be found in Fig. 10.

Some of the information contained in Table IV has been also plotted in Figs. 11(a) and 11(b), where one can observe the density trend of ω_α and ϕ_α, respectively. The main feature in Fig. 11(a) is the presence of a D_2 high-frequency mode (HFM), ω_{hf,D_2}, for $0\% < x_{D_2} < 60\%$, whose frequency decreases with increasing the deuterium concentration (full red circles with black rings). Slightly above, the corresponding Ne high-frequency mode, $\omega_{hf,Ne}$, is visible in the same x_{D_2} range, showing, with exception of sample No. (II), an opposite trend, i.e., increasing along with the deuterium concentration (empty blue squares with green fillings). In addition, one can also observe two low-frequency modes (LFMs), $\omega_{lf,Ne}$ and ω_{lf,D_2}, one belonging to Ne (empty blue squares) and the other to D_2 (full red circles with no rings), which initially exhibit very similar frequency values, even though the former decreases with x_{D_2}, while the latter seems more or less constant. For $x_{D_2} > 60\%$, the frequency behavior changes: the two couples, ω_{lf,D_2} and ω_{hf,D_2} on one side and $\omega_{lf,Ne}$ and $\omega_{hf,Ne}$ on the other, simply disappear, leaving room to single modes for both species (symbols with crosses), which, however, exhibit a different behavior: the D_2 frequencies turn out to be almost constant, while the Ne ones seem to rapidly grow, even though their determination becomes less precise as shown by the large error bars.

At this stage, at least for $0\% < x_{D_2} < 60\%$, one is surely tempted, in the spirit of IO, to associate the D_2 HFMs to the rattling of deuterium molecules in the pseudocages, while the D_2 and Ne LFMs would somehow represent the pseudocage motion in the bulk liquid. To this end, it might be reasonable to introduce a new LFM frequency $\overline{\omega}_{lf}$, given by a weighted mean of ω_{lf,D_2} and $\omega_{lf,Ne}$ based, for instance, on the mixture concentration. The frequency ratio between the D_2 HFM and the weighted mean LFM, dubbed $R_{h-l} = \omega_{hf,D_2}/\overline{\omega}_{lf}$, is not constant in the $0\% < x_{D_2} < 60\%$ range, where it varies from 2.27 ± 0.02 to 3.9 ± 0.3. As we have seen above, it entails that, in the case of a D_2 rattling molecule, the corresponding pseudocage mass, $M_{1,D_2} \approx R^2_{h-l} M_{D_2}$, varies from $M_{1,D_2} = (20.7 \pm 0.4)$ amu to (60 ± 8) amu. Dividing by the average molecular weight of each mixture, estimated as $\mathcal{N}_{D_2}(n)(M_{D_2} x_{D_2} + M_{Ne} x_{Ne})$, one can approximately evaluate the number of particles, $\mathcal{N}_{D_2}(n)$, forming the pseudocage around D_2: from 1.16 ± 0.02 molecules for sample No. II to 5.4 ± 0.7 for sample No. VII. These figures, although more

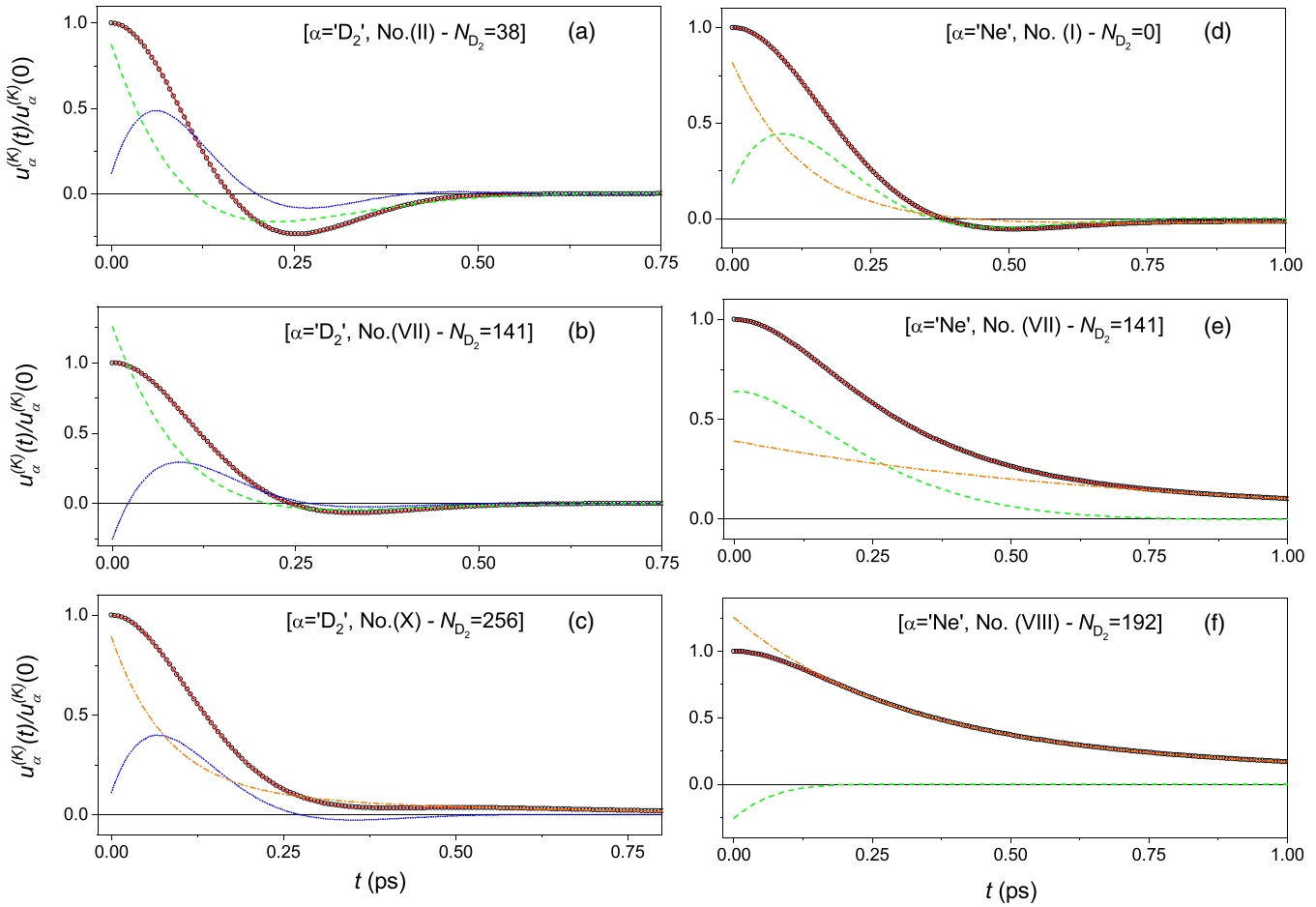

FIG. 10. Selected examples of the canonical VACFs, $u_\alpha^{(K)}(t)$ (with $\alpha =$ Ne or D_2), obtained from CMD simulations (black empty circles), together with their best fits using the EET approach (red full lines). Five concentrations have been included among those reported in Table I, namely No. I [panel (d)], No. II [panel (a)], No. VII [panels (b) and (e)], No. VIII [panel (f)], and No. X [panel (c)]. Panels (a), (b), and (c) contain the $u_{D_2}^{(K)}(t)/u_{D_2}^{(K)}(0)$ plots and panels (d), (e), and (f) the $u_{Ne}^{(K)}(t)/u_{Ne}^{(K)}(0)$ ones. In this way, spectra have been normalized (i.e., their values at $t = 0$ ps are set equal to 1.0) for graphic reasons. Propagating EET components have been also plotted following the notation of Table IV: green dashed lines stand for the 1st C modes, while blue dotted lines stand for the 2nd C modes. Diffusive modes have been combined and plotted as orange dot-dashed lines when present.

physically meaningful than the original IO results, are still far from the reported SPCF estimates ($12.67 > \mathcal{N}_{D_2}(n) > 11.64$) and, in addition, exhibit the wrong trend with n. As we will see in the conclusions, this result actually disproves the applicability of the IO model to our binary mixture systems.

For $0\% < x_{D_2} < 60\%$, Fig. 11(b) shows the phase of the four modes, indicating that $\phi_{lf,Ne}$ and ϕ_{hf,D_2} are generally both negative and quite close to each other, while ϕ_{lf,D_2} is mildly positive, and $\phi_{hf,Ne}$ is strongly positive. In other words, the two LFMs often have similar frequencies, but they are largely dephased between each other (more than $\pi/2$). Also this fact seems in contradiction with the IO model interpretation proposed above, since D_2 and Ne, when forming the same pseudocage, should oscillate in phase since they belong to a relatively rigid structure. On the contrary, one might expect that ϕ_{hf,D_2}, if associated with a D_2 rattling, would exhibit a certain shift with respect to the two LFM phase values; but this is not the case. For this reason, it appears more reasonable to explain the shift between ϕ_{lf,D_2} and ϕ_{hf,D_2} on one side, and between $\phi_{lf,Ne}$ and $\phi_{hf,Ne}$ on the other, as a sort of liquid equivalent of what can be easily observed in a non-Bravais solid crystal made of two components with uneven masses, where the distinct phonon branches (either acoustic or optic) projected on the different species (either Ne or D_2) can show quite a large phase difference among one another [53]. Moving to $x_{D_2} > 60\%$ one notes that the deuterium phases are almost constant and close to the $\phi_{lf,Ne}$ values observed for lower values of x_{D_2}, while the Ne ones grow rapidly and, somehow surprisingly, are not distant from the $\phi_{hf,Ne}$.

Finally, an additional clue can be gained by comparing the present ω_j values with the simulated dispersion curves, $\Omega_{d,Ne}(q)$ and $\Omega_{d,D_2}(q)$, obtained from the maxima of the longitudinal current-current correlation spectra, $\tilde{c}_L(q,\omega)$, and reported in Fig. 15 of Ref. [13]. Although only three x_{D_2} values of those plotted in this figure are of interest to us, namely $x_{D_2} = 0\%$, 23%, and 49%, roughly corresponding to the present Nos. I, III, and V–VI, one can note a strict correspondence between $\Omega_{d,Ne}(q)$ and $\omega_{lf,Ne}$ on one side, as well as $\Omega_{d,D_2}(q)$ and ω_{hf,D_2} on the other. However, as for ω_{lf,D_2} and $\omega_{hf,Ne}$, which are both associated with rather weak EET amplitudes [54], we are in the position neither to unambiguously assign the origin of these modes nor to find a

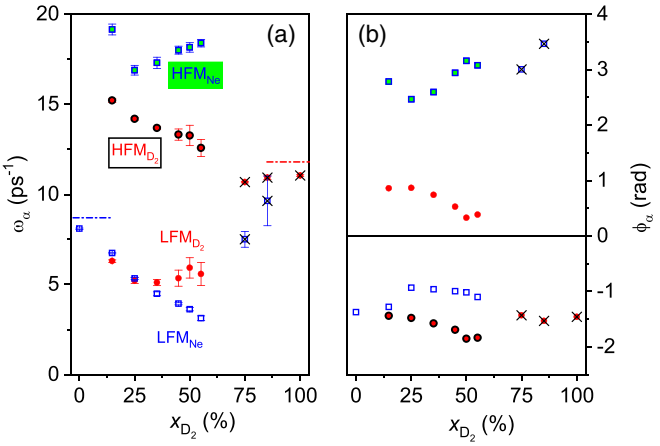

FIG. 11. The EET fitting results from Table IV, concerning frequencies ω_α and phases ϕ_α (with $\alpha =$ Ne or D_2), are plotted as a function of x_{D_2} in panels (a) and (b), respectively. Red full circles represent D_2, while blue empty squares stand for Ne. For $0\% < x_{D_2} < 60\%$, black rings and green fillings are used to distinguish the high-frequency 2nd C modes (HFMs) from their low-frequency counterpart (LFM) for D_2 and Ne, respectively; while, for $x_{D_2} > 60\%$, such a distinction disappears and both frequencies and phases are marked by black crosses. The horizontal dash-dotted lines in panel (a) mark the experimental coherent scattering results from Refs. [55,56] for pure liquid Ne and D_2, respectively. Available statistical uncertainties are plotted as error bars.

simple correspondence with the peaks contained in $\tilde{c}_L(q,\omega)$. In addition, it is worth mentioning the experimental estimates, obtained from coherent inelastic scattering, of the longitudinal frequencies in pure samples of Ne and D_2. The maxima (with respect of q) of these dispersion curves clearly support the quality of the present EET data analysis if compared with the fit results in Fig. 11(a). Namely, in the case on Ne, Ref. [55] reports the maximum of $\Omega_L(q)$ at about (5.7 ± 1.5) meV, corresponding to (8.7 ± 2.3) ps^{-1}, in a sample at $T = 32$ K and $n = 34.7$ nm^{-3}; while, as for D_2, where data close to our thermodynamic conditions are unfortunately missing, one can approximately scale the frequency data from Ref. [56] (taken at $T = 20.7$ K and $n = 25.4$ nm^{-3}) making use of the appropriate speed of sound values [57] (i.e., $c_s = 984$ m/s for Ref. [56] and $c_s = 778$ m/s for the present sample No. X), obtaining $\omega_{D_2} \approx 11.8$ ps^{-1}. The agrement of both estimates with the EET frequency results for pure samples Nos. I and X is really impressive.

IV. CONCLUSIONS

In this work we have presented new and original VACF data of liquid D_2 mixed with liquid Ne for several values of x_{D_2}, using the static and dynamic quantum simulation methods PIMC [31] and CMD [33]. We have shown that CMD can perfectly reproduce the $\langle E_K \rangle$ of both molecular species, and gives substantially correct estimates of the corresponding Ω_E, confirming the effectiveness of this semi-quantum technique when dealing with correlations of operators which, like the VACF, are linear in the particle positions or momenta [58]. This permitted us to confidently address the extraction of other physical information by means of fits to the various canonical VACF spectra, which, differently from the truly quantum ones, still retain a number of characteristics allowing for the use of standard classical models. We have utilized two types of heuristic fit models introduced in the literature a long time ago (i.e., LV and IO), as well as the more recent, theoretically based EET modeling. In particular, we have found that the LV model [42], which is considered as very flexible and rather heuristic, provides a good spectral description of the Kubo correlation for both molecular species in the full x_{D_2} (and n) range. In addition, its binary collision component, which dominates at short times (linked with the large ω values in the spectra), reproduces reasonably well the first two terms of the power series expansion of the normalized canonical VACFs, the latter term being simply Ω_E. As for the effective many-body term in the LV model, which, on the contrary, is the crucial part at long times, we found that it often turns out to be negative, causing a change in sign of the LV memory function at times larger than a certain threshold. Unfortunately, the meaning of such a peculiar result was not easy to interpret since the LV many-body term is not grounded on a solid physical theory but stems from some mathematical constraints imposed in an *ad hoc* way. For these reasons, we have resorted to two versions (the more complete IO, and the more primitive CE) of a totally different approach to the VACF based on the concept of an "itinerant oscillator" [44] which, in spite of its simplicity, retains a certain physical background at least for very dense fluids. Indeed, it is based on the interaction between an individual molecule rattling inside a short-lived pseudocage, temporarily formed by the neighbor particles and diffusing in the bulk liquid. The SPCFs from PIMC provided all the ingredients to accurately calculate the average properties of such pseudocages, including, in particular, their mass M_1 as a function of the rattling particle mass M_0 and the system x_{D_2} (or n). The main characteristic of this class of models is the fact that, due to the supposed free diffusion of the pseudocages in the bulk, the ratio ω_0^2/ω_1^2 between the squared rattling frequency, ω_0^2, and the squared oscillation frequency of the short-lived particle aggregates, ω_1^2, should be rigorously identical to the inverse mass ratio M_1/M_0. Already the simplistic CE model, which can be devised even without performing complete VACF fits, showed that the M_1 estimates from PIMC and CMD were utterly irreconcilable since they disagreed by more than one order of magnitude for both M_0 values. This result was extremely surprising since it also turned out that $M_1 < M_0$ (i.e., the pseudocage was on average lighter than the rattling particle!), similarly to what had been found many years ago analyzing classical liquid Ar simulations. To clarify this issue, a detailed IO fitting procedure was also carried out, providing a fairly good description of the CMD data, which, unsurprisingly, became particularly effective in the case of D_2 at low values of x_{D_2}, where the IO fit quality was better than (or comparable to) the LV one. However, as far as M_1/M_0 was concerned, the new and supposedly more accurate estimates were even farther from the PIMC results than the corresponding CE estimates, with unrealistic mean values for M_1 in both the Ne and D_2 cases. Therefore, despite its good practical capability to fit canonical VACFs of dense quantum binary systems, the IO model contains strong intrinsic limitations which make the numerical

values of its fitting parameters physically implausible. We are strongly inclined to think that the IO failure has a clear origin: the motion of the pseudocage is supposed to be a free diffusion in the bulk, with the vibrational component coming only from the reaction to the rattling particle inside the nearest neighbor pseudocage itself. However, in a dense fluid also the second- and third-neighbor shells likely exert an effect on the nearest neighbor one, thus modifying the force constant accounting for the pseudocage vibrations. Since such an effect would be understandably different for the pseudocage and the rattling particle inside it, the translational invariance would be broken and the action-reaction principle would not apply in the way we discussed in the text. This would imply the possibility of the existence of two distinct force constants, κ_0 and κ_1, and, consequently, $(\omega_0/\omega_1)^2 \neq M_1/M_0$, explaining the breakdown of the IO model.

The final part of this study was dedicated to the EET, a more modern, physically grounded, and comprehensive approach to the analysis of the VACFs, in which a correlation function is decomposed into a sum of a small number of exponential modes, either of propagating or diffusive type. The EET method was very successful for both molecular species at all the n values. In particular, in the $10\% \leqslant x_{D_2} < 60.0\%$ range, the interpretation of the obtained results turned out to be quite straightforward in terms of propagating modes: both Ne and D_2 were characterized by two kinds of modes: LFMs (i.e., $\omega_{lf,\mathrm{Ne}}$ and ω_{lf,D_2}) and HFMs (i.e., $\omega_{hf,\mathrm{Ne}}$ and ω_{hf,D_2}). The first and the last excitation frequencies were found in excellent agreement with the pseudodispersion curves obtained from the collective dynamical simulations of similar Ne-D_2 mixtures [13]. It is reasonable to assume that LFMs and HFMs correspond to acoustic and optic vibrations, respectively. On the contrary, if the mode frequencies determined by EET are used to estimate the pseudocage masses as in the IO framework, we find values much smaller than the mentioned SPCF estimates ($10 - 12$ molecules per pseudocage) and, moreover, with an incorrect dependence on n. In our opinion these findings definitely prove that the whole concept of individual particles rattling inside short-lived pseudocages formed by their neighbors is intrinsically flawed, at least from a dynamic point of view. In fact, this seems to be the case even in the most favorable scenario, i.e., where a small amount of D_2 impurities are dispersed in a Ne-rich mixture.

ACKNOWLEDGMENTS

This work has been partially funded by the Next Generation EU Project No. PRIN-2022JWAF7Y. One of the authors (M.N.) thanks Walter Penits (Universität Wien, Austria) for his interest and kind assistance with the computer simulations.

APPENDIX A: CHECKING PIMC AND CMD SIMULATIONS FOR POSSIBLE FINITE-SIZE EFFECTS

In this Appendix we will focus on the following Ne-D_2 mixture: 85.16% Ne + 14.84% D_2 (with a molecular density $n = 30.71$ nm^{-3} at a temperature $T = 30.0$ K) to test the stability of our results when either the number of particles N or the Trotter number P (see Sec. II for details) is varied. The choice of such a mixture is justified by the fact that it corresponds to sample No. II (see Table I) which is the most unbalanced of all the simulated binary mixtures, with the lowest value of D_2 concentration. This means that in this case, at least in theory, the deuterium self-dynamics should not only be the most prone to the so-called "finite-size effects" but should also show the most pronounced quantum behavior, due to the high overall density of the mixture.

Test calculations on the three static pair correlation functions (SPCFs, i.e., those concerning Ne-Ne, Ne-D_2, or D_2-D_2) using the PIMC technique have been carried out in the case of the selected mixture. We have used a total number of particles, namely $N = 512$, which is twice that of our standard PIMC simulations ($N = 256$) presented in the paper. This choice implied the presence of 436 Ne atoms and 76 D_2 molecules instead of 218 Ne atoms and 38 D_2 molecules only, as in the previous PIMC calculation. In both simulations the Trotter number P was kept fixed to 32. Three relevant physical quantities have been explicitly evaluated and compared: the mean kinetic energy per particle for both species ($\alpha =$ Ne or D_2) $\langle E_K\rangle_\alpha$, which is already a standard PIMC output, as well as the Einstein frequencies $\Omega_{E,\alpha}$, and the mean-square forces $\langle \mathbf{F}^2\rangle_\alpha$, which, on the contrary, must be derived from the SPCFs in connection with the Laplacians and square gradients of the three interparticle potentials [see Eq. (B5) in Appendix B]. A similar test was also performed on the same selected mixture keeping the particle number constant ($N = 256$), but doubling the Trotter number P from 32 to 64. Also in this case, the three relevant physical quantities mentioned above have been evaluated and compared. The results of both types of PIMC tests (i.e., on either N or P) are reported in Table V, where one can see that by doubling either the number of particles or the Trotter number, the relative variations of $\langle E_K\rangle_{\mathrm{Ne}}$, $\Omega_{E,\mathrm{Ne}}$, and $(\langle \mathbf{F}^2\rangle_{\mathrm{Ne}})^{0.5}$ are not larger than 0.08%, 0.2%, and 0.2%, respectively; while those of $\langle E_K\rangle_{D_2}$, Ω_{E,D_2}, and $(\langle \mathbf{F}^2\rangle_{D_2})^{0.5}$ are not larger than 0.2%, 0.3%, and 0.2%, respectively.

Test calculations on the two types of VACFs (i.e., those concerning either Ne or D_2) using the CMD technique have been carried out in the case of the selected mixture. We have used a number of particles, namely $N = 1024$, which is four times that of our standard CMD simulations ($N = 256$) presented in the paper. This choice implied the presence of 872 Ne atoms and 152 D_2 molecules instead of 218 Ne atoms and 38 D_2 molecules only, as in the previous CMD calculation. In both simulations the Trotter number P was kept fixed to 32. The outputs of both CMD calculations are plotted in Fig. 12. While no changes can be discerned on the scale of the graphs, three relevant physical quantities have been explicitly evaluated and compared: the mean kinetic energy per particle of both species ($\alpha =$ Ne or D_2) $\langle E_K\rangle_\alpha$, their Einstein frequencies $\Omega_{E,\alpha}$, and their mean-square forces $\langle \mathbf{F}^2\rangle_\alpha$. It is worth noting that while $\Omega_{E,\alpha}$ can be derived directly from the CMD outputs, i.e., the Kubo-transformed (or canonical) VACFs $u_\alpha^{(K)}(t)$, the other two physical quantities, $\langle E_K\rangle_\alpha$ and $\langle \mathbf{F}^2\rangle_\alpha$, have to be extracted from the velocity autocorrelation spectra obtained via a Fourier transform of the canonical VACFs [see Eq. (B1) in Appendix B]. A similar test was performed on the same selected mixture, but now keeping the particle number constant ($N = 256$) and doubling the Trotter number P from 32 to 64. The outputs of both CMD calculations are also plotted in Fig. 12. Also in this case, the three relevant physical quantities

TABLE V. Results from the tests of the effect of finite total number of particles N and Trotter number P on our PIMC calculations with deuterium concentration $x_{D_2} = 14.84\%$, molecular density $n = 30.71$ nm^{-3}, and temperature $T = 30.0$ K, including the mean kinetic energy per particle for both species $\langle E_K\rangle_\alpha$ (α = Ne or D_2), as well as the Einstein frequencies $\Omega_{E,\alpha}$, and the mean-square forces $\langle \mathbf{F}^2\rangle_\alpha$. Statistical uncertainties have been reported in parentheses.

N	P	$k_B^{-1}\langle E_K\rangle_{Ne}$ (K)	$k_B^{-1}\langle E_K\rangle_{D_2}$ (K)	$\hbar\Omega_{E,Ne}$ (meV)	$\hbar\Omega_{E,D_2}$ (meV)	$(\langle \mathbf{F}^2\rangle_{Ne})^{0.5}$ (meV/Å)	$(\langle \mathbf{F}^2\rangle_{D_2})^{0.5}$ (meV/Å)
256	32	52.70(1)	72.40(1)	4.021(3)	8.347(2)	34.35(2)	37.577(8)
512	32	52.74(1)	72.26(3)	4.028(3)	8.375(5)	34.41(3)	37.51(2)
256	64	52.74(6)	72.54(6)	4.02(2)	8.35(1)	34.4(1)	37.64(5)

have been evaluated and compared. The results of both types of CMD tests are reported in Table VI, where one can see that by either quadrupling the number of particles or doubling the Trotter number, the relative variations of $\langle E_K\rangle_{Ne}$, $\Omega_{E,Ne}$, and $(\langle \mathbf{F}^2\rangle_{Ne})^{0.5}$ are not larger than 0.04%, 0.07%, and 0.2%, respectively; while those of $\langle E_K\rangle_{D_2}$, Ω_{E,D_2}, and $(\langle \mathbf{F}^2\rangle_{D_2})^{0.5}$ are not larger than 0.3%, 0.5%, and 0.6%, respectively.

APPENDIX B: TESTING THE CMD RESULTS

In this Appendix, exploiting the knowledge of the partial SPCFs, we will perform three important tests on $\tilde{u}_\alpha^{(K)}(\omega)$ and $\tilde{u}_\alpha(\omega)$ making use of their moments which can be simply transformed into four important physical quantities [59], namely T, $\langle E_K\rangle_\alpha$, the Einstein frequency $\Omega_{E,\alpha}$, and the mean-squared force $\langle \mathbf{F}^2\rangle_\alpha$, for both species Ne and D_2:

$$
\begin{aligned}
M_\alpha^{-1} k_B T &= \int_{-\infty}^{\infty} d\omega\, \tilde{u}_\alpha^{(K)}(\omega) = u_\alpha^{(K)}(t=0),\\
\frac{2}{3} M_\alpha^{-1} \langle E_K\rangle_\alpha &= \int_{-\infty}^{\infty} d\omega\, \tilde{u}_\alpha(\omega),\\
M_\alpha^{-1} k_B T\, \Omega_{E,\alpha}^2 &= \int_{-\infty}^{\infty} d\omega\, \omega^2\, \tilde{u}_\alpha^{(K)}(\omega) = -\ddot{u}_\alpha^{(K)}(t=0),\\
\frac{1}{3} M_\alpha^{-2} \langle \mathbf{F}^2\rangle_\alpha &= \int_{-\infty}^{\infty} d\omega\, \omega^2\, \tilde{u}_\alpha(\omega).
\end{aligned}
\tag{B1}
$$

It is important to stress that in a classical scenario the second physical quantity is simply related to the first, and the fourth physical quantity to the third [40,60]: $\langle E_K\rangle_\alpha = \frac{3}{2} k_B T$

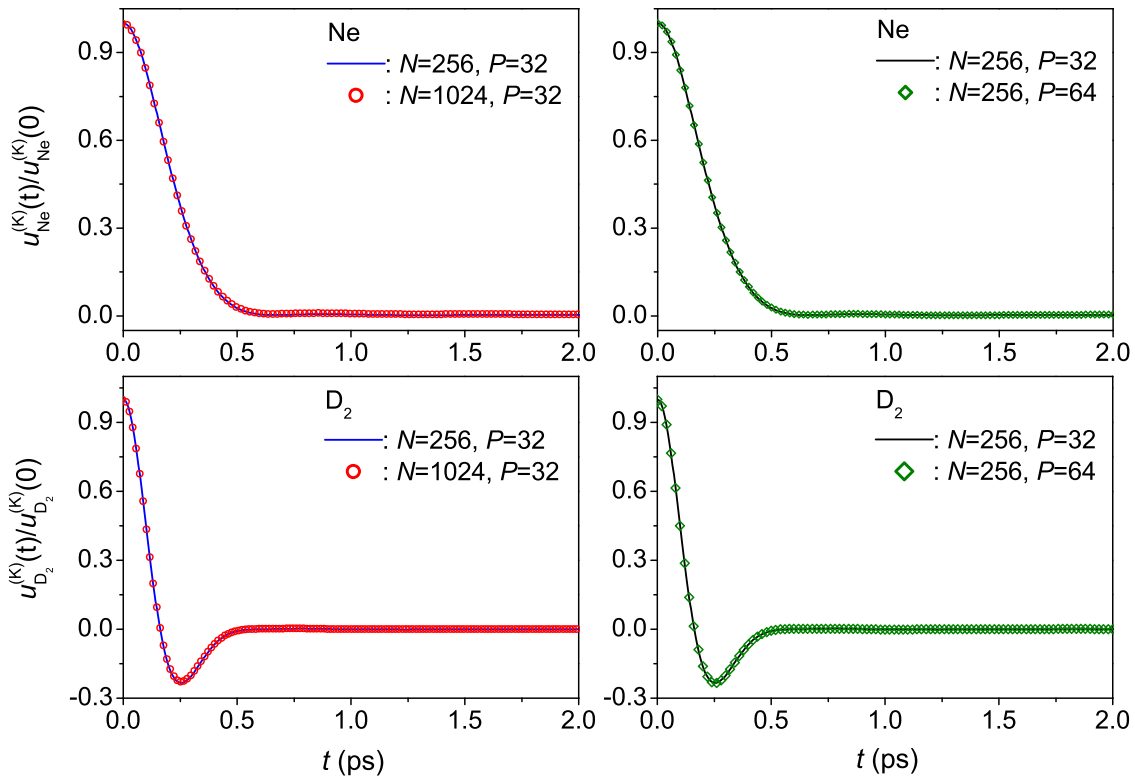

FIG. 12. Kubo-transformed velocity autocorrelation functions $u_\alpha^{(K)}(t)$ (with α = Ne or D_2), obtained from CMD for a test binary mixture ($x_{D_2} = 14.84\%$, molecular density $n = 30.71$ nm^{-3}, temperature $T = 30.0$ K). Upper panels refer to Ne, while lower panels to D_2. Full lines (either blue or black) represent the outputs evaluated with $N = 256$ and $P = 32$, red empty circles stand for those obtained with $N = 1024$ and $P = 32$, and green empty diamonds for those obtained with $N = 256$ and $P = 64$.

TABLE VI. Results from the tests of the effect of finite total number of particles N and Trotter number P on our CMD calculations with deuterium concentration $x_{D_2} = 14.84\%$, molecular density $n = 30.71$ nm^{-3}, and temperature $T = 30.0$ K, including the mean kinetic energy per particle for both species $\langle E_K\rangle_\alpha$ ($\alpha =$ Ne or D_2), as well as the Einstein frequencies $\Omega_{E,\alpha}$, and the mean-square forces $\langle \mathbf{F}^2\rangle_\alpha$. Statistical uncertainties have been reported in parentheses.

N	P	$k_B^{-1}\langle E_K\rangle_{Ne}$ (K)	$k_B^{-1}\langle E_K\rangle_{D_2}$ (K)	$\hbar\Omega_{E,Ne}$ (meV)	$\hbar\Omega_{E,D_2}$ (meV)	$(\langle \mathbf{F}^2\rangle_{Ne})^{0.5}$ (meV/Å)	$(\langle \mathbf{F}^2\rangle_{D_2})^{0.5}$ (meV/Å)
256	32	52.82(1)	72.52(5)	3.973(1)	7.896(5)	31.593(8)	32.83(2)
1024	32	52.801(9)	72.28(3)	3.9707(7)	7.859(3)	31.534(5)	32.64(1)
256	64	52.798(4)	72.48(1)	3.9709(3)	7.892(1)	31.547(3)	32.829(5)

and $\langle \mathbf{F}^2\rangle_\alpha = 3M_\alpha k_B T\,\Omega_{E,\alpha}^2$. This is due to the fact that in the classical limit $\tilde{u}_\alpha^{(K)}(\omega)$ and $\tilde{u}_\alpha(\omega)$ coincide.

In Fig. 13 one can observe a generally good agreement between $M_\alpha k_B^{-1} u_\alpha^{(K)}(t=0)$ and the prescribed simulation temperature T for both species, even though the lighter molecules (i.e., D_2) tend to be slightly "warmer" than the heavier ones (i.e., Ne). This small equipartition defect has a clear redistributional origin since the overall system thermostatting is perfect as shown in this figure by the two pure cases (i.e., $x_{D_2} = 0\%$ or 100%). To cure this slight velocity mismatch between Ne and D_2, $\tilde{u}_\alpha^{(K)}(\omega)$ and $\tilde{u}_\alpha(\omega)$ have been both corrected through the factor $M_\alpha^{-1} k_B T / u_\alpha^{(K)}(t=0)$. So, from now on, only corrected VACF spectra will be dealt with in the present work. The effect of such a correction on the self-diffusion coefficients D_{Ne} and D_{D_2}, whose raw estimates were reported in Table I, is visible, although rather minute, in Fig. 5. In addition, it is worth noticing that a typical diffusional behavior can be clearly observed in our quantum calculations: both D_{Ne} and D_{D_2} rapidly decrease as n grows with x_{Ne} (where $x_{Ne} = 1 - x_{D_2}$). However, one can also see that the more x_{D_2} approaches zero, the closer D_{Ne} and D_{D_2} become. This effect might be explained by the fact that in a dense liquid the diffusion of the few D_2 molecules is dominated by that of the more abundant and heavier Ne atoms which completely surround the lightweight particles hindering their motion [61]. Moving to the quantum mechanical mean kinetic energies $\langle E_K\rangle_\alpha$ in Fig. 14, where the values obtained from the CMD simulations via the second formula of Eq. (B1) are compared with the corresponding PIMC results reported in Table I, one can note an excellent agreement for both molecular species, proving that the "mean-squared velocity correction" mentioned above has been beneficial. This comparison can be considered as an important test of the consistency of the CMD procedure since the two sets of values have a thoroughly different origin: $\langle E_K\rangle_\alpha$ from PIMC, as obtained via the "crude energy estimator," is related to the average squared distance between successive monomers on the ring-polymer which isomorphically represents a quantum particle (either Ne or D_2), while in the CMD case the same quantities are derived from the area of the quantum VACF spectra which, on the contrary, are linked with the dynamics of the centroids of the various polymers. In all the systems investigated, both Ne and D_2 exhibit sizable quantum effects as proved by the fact that $\langle E_K\rangle_\alpha$ is always quite larger than the classical translational mean kinetic energy (i.e., $\frac{3}{2}T = 45$ K). To be more quantitative, one can extract $\Theta_{D,\alpha}$ from all the $\langle E_K\rangle_\alpha$ values reported in Table I via the well-known Debye-model formula [8]:

$$\langle E_K\rangle_\alpha = \frac{9}{4}\int_0^{k_B\Theta_{D,\alpha}} \left(\frac{\hbar\omega}{k_B\Theta_{D,\alpha}}\right)^3 \coth\left(\frac{\hbar\omega}{2k_BT}\right) d\hbar\omega, \quad \text{(B2)}$$

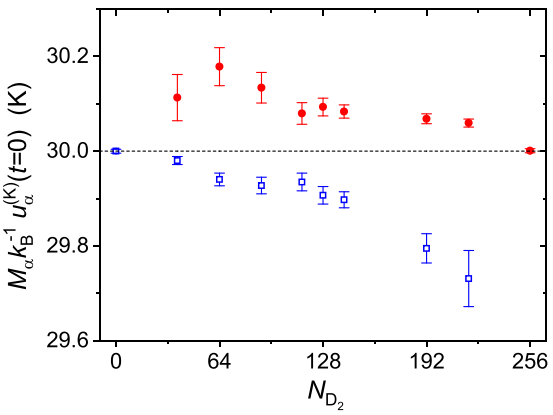

FIG. 13. Effective temperature $M_\alpha k_B^{-1} u_\alpha^{(K)}(t=0)$ (with $\alpha =$ Ne or D_2) as a function of N_{D_2}, obtained from CMD simulations compared with the prescribed temperature T. Blue empty squares with error bars represent Ne, while red full circles with error bars stand for the D_2 center of mass. Black dashed line marks the T level. See Table I for further details.

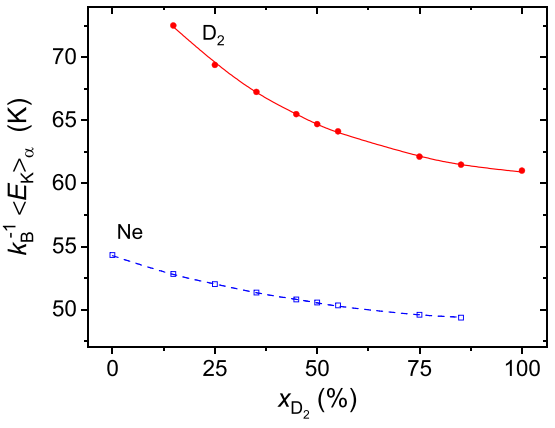

FIG. 14. Single-particle mean kinetic energy values $k_B^{-1}\langle E_K\rangle_\alpha$ (with $\alpha =$ Ne or D_2) as a function of x_{D_2} obtained from CMD simulations compared with the corresponding PIMC results reported in Table I. Blue empty squares and blue dashed line stand for Ne, while red full circles and red full line stand for the D_2 center of mass. Lines are splines through the PIMC data, while symbols refer to CMD estimates, whose statistical errors are smaller than the symbol size.

from which one can also obtain the corresponding zero-point mean kinetic energy $\frac{9}{16}k_B\Theta_{D,\alpha}$, which has a purely quantum nature. It is straightforward to verify in Table I that $\Theta_{D,\alpha} > T$ for all samples and for both molecular species. This proves the quantum character of the fluid systems under investigation in a rigorous way [7]. In addition, from the variation of $\Theta_{D,\mathrm{Ne}}$ and $\Theta_{D,\mathrm{D_2}}$ as a function of the total molecular volume n^{-1}, it is possible to extract the two Grüneisen parameters [8] for the Debye temperature, labeled $\gamma_{D,\alpha}$:

$$\gamma_{D,\alpha} = -\frac{n^{-1}}{\Theta_{D,\alpha}}\left(\frac{\partial\Theta_{D,\alpha}}{\partial n^{-1}}\right)_T = \frac{n}{\Theta_{D,\alpha}}\left(\frac{\partial\Theta_{D,\alpha}}{\partial n}\right)_T, \tag{B3}$$

which amount to 0.83 ± 0.02 and 0.827 ± 0.009 for Ne and D_2, respectively. These two figures appear to be in line with the Grüneisen parameter value of a nonpolar fluid at a density rather lower than its triple-point value [62].

We have seen that $\langle E_K\rangle_\alpha$ was directly calculated by our PIMC code, while the Einstein frequency and the mean-squared force were not. However, the latter two can be generally estimated exploiting the SPCF, $g(r)$, if the interparticle potential, $v(r)$, is assumed to be isotropic and pairwise additive [1]:

$$M\Omega_E^2 = \frac{n}{3}\int g(r)[\nabla^2 v(r)]d^3\mathbf{r},$$
$$\langle\mathbf{F}^2\rangle = n\int g(r)[\nabla v(r)]^2 d^3\mathbf{r}. \tag{B4}$$

Nevertheless, in the case of a binary mixture the standard relationships above turn out to be slightly more complicated since they include the three partial $g_{\alpha,\beta}(r)$ and the three interparticle potentials $v_{\alpha,\beta}(r)$. After some straightforward algebraic manipulations, one can generalize Eq. (B4) as follows:

$$M_\alpha\Omega_{E,\alpha}^2 = \frac{x_\alpha n}{3}\int g_{\alpha,\alpha}(r)[\nabla^2 v_{\alpha,\alpha}(r)]d^3\mathbf{r} + \frac{x_\beta n}{3}\int g_{\alpha,\beta}(r)[\nabla^2 v_{\alpha,\beta}(r)]d^3\mathbf{r},$$
$$\langle\mathbf{F}^2\rangle_\alpha = x_\alpha n\int g_{\alpha,\alpha}[\nabla v_{\alpha,\alpha}(r)]^2 d^3\mathbf{r} + x_\beta n\int g_{\alpha,\beta}[\nabla v_{\alpha,\beta}(r)]^2 d^3\mathbf{r}, \tag{B5}$$

where x_α (or $x_\beta = 1 - x_\alpha$) represent the concentration of α-type (or β-type) molecules. The SPCF-derived results for $\hbar\Omega_{E,\alpha}$ and $(\langle\mathbf{F}^2\rangle_\alpha/3)^{1/2}$ are displayed in Figs. 6 and 15, respectively.

In the former figure one can observe a fairly good agreement between the two estimates of $\hbar\Omega_{E,\alpha}$ for both species, even though a general tendency of the CMD to underestimate the Einstein frequency values clearly shows up. However, in analogy with what has been found in Fig. 13 for the "effective temperature," such an agreement is almost perfect in the case of the two pure systems [i.e., samples Nos. I and X], while it somehow deteriorates for the α species as the respective number of molecules N_α decreases. For this reason we cannot completely rule out an alternative explanation, although it seems very unlikely (as suggested in Appendix A): namely, the possibility that the mentioned small inaccuracies are caused by the numerical implementation of Eq. (B5) via the SPCFs calculated by our PIMC code. Moving to Fig. 15 a different scenario appears as far as $\langle\mathbf{F}^2\rangle_\alpha$ is concerned: the general CMD underestimation can be appreciated even in the case of the two pure samples Nos. I and X, which, however, still exhibit the best agreements between the two techniques. In this respect, it can be also observed that CMD, differently from PIMC, provides $(\langle\mathbf{F}^2\rangle_\alpha/3)^{1/2}$ values which are almost identical for the two species. However, at the moment, we have no explanation for this effect. In spite of such a minor discrepancy, one should note that both approaches (i.e., CMD and PIMC) capture quite well the quantum character of the mean-squared force in our mixtures, as clearly shown by their large difference from the two purely classical components, $M_\alpha k_B T\,\Omega_{E,\alpha}^2$, also reported in the figure. In this respect, it is also interesting to note that the possible introduction of a sort of "quantum enhanced temperature" (i.e., $T_\alpha^* = \frac{2}{3}k_B^{-1}\langle E_K\rangle_\alpha > T$) into the aforementioned classical formula for $\langle\mathbf{F}^2\rangle_\alpha$ is not sufficient to reproduce the fully quantum values of the mean-squared force.

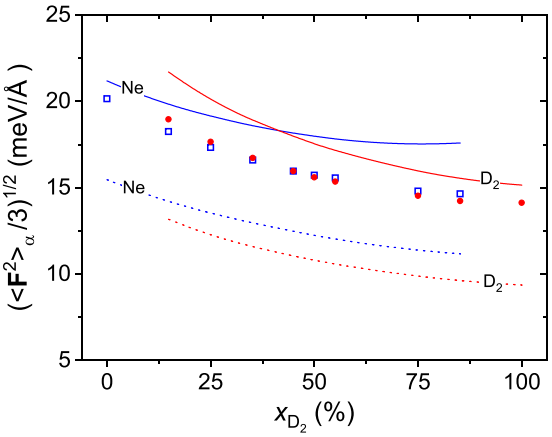

FIG. 15. Root-mean-squared force values $(\langle\mathbf{F}^2\rangle_\alpha/3)^{1/2}$ (with α = Ne or D_2) as a function of x_{D_2} obtained from CMD simulations compared with the corresponding results derived from mean-squared potential gradients and SPCFs via Eq. (B5). Classical limits are also reported as dashed lines. Blue color stands for Ne, while red color stands for the D_2 center of mass. Full lines are splines through the PIMC/SPCF-based data, while symbols (empty for Ne, full for D_2) refer to CMD estimates, whose statistical errors are smaller than the symbol size. Dashed lines are also splines and are obtained using the PIMC/SPCF-based data for $\hbar\Omega_{E,\alpha}$ plotted in Fig. 6.

[1] J. P. Hansen and I. R. McDonald, *Theory of Simple Liquids: with Applications to Soft Matter*, 4th ed. (Academic Press, Cambridge, MA, 2013).
[2] A. Griffin, *Excitations in a Bose-condensed Liquid* (Cambridge University Press, Cambridge, UK, 1993).
[3] H. R. Glyde, *Excitations in Liquid and Solid Helium* (Clarendon Press, Oxford, UK, 1995).
[4] V. V. Ignatyuk, I. M. Mryglod, and M. V. Tokarchuk, Low Temp. Phys. **25**, 295 (1999).
[5] J. D. Pandey, Acoustics Lett. **3**, 90 (1979).

[6] R. D. McCarty, J. Hord, and H. M. Roder, *Selected Properties of Hydrogen*, Natl. Bur. Stand. (U.S.) Monograph No. 168 (U.S. GPO, Washington, DC, 1981).

[7] A. F. Andreev, Zh. Eksp. Teor. Fiz. **28**, 603 (1978) [JETP Lett. **28**, 556 (1978)].

[8] D. C. Wallace, *Thermodynamics of Crystals* (Dover Publications, Mineola, NY, 2003).

[9] J. P. Boon and P. A. Fleury, J. Phys. Colloques **33**, C1-19 (1972).

[10] J. Bigeleisen, J. Chem. Phys. **39**, 769 (1963).

[11] M. Ceriotti, W. Fang, P. G. Kusalik, R. H. McKenzie, A. Michaelides, M. A. Morales, and T. E. Markland, Chem. Rev. **116**, 7529 (2016).

[12] S. W. Lovesey, *Theory of Neutron Scattering from Condensed Matter* (Clarendon Press, Oxford, UK, 1986), Vol. I.

[13] D. Colognesi, U. Bafile, E. Guarini, T. Guidi, and M. Neumann, Phys. Rev. E **105**, 054603 (2022).

[14] H. L. Frisch and Z. W. Salsburg (eds.) *Simple Dense Fluids* (Academic Press, New York, NY, 1968), p. 289.

[15] V. F. Sears, Proc. Phys. Soc. **86**, 953 (1965).

[16] W. T. Coffey and M. E. Walsh, J. Chem. Phys. **106**, 7625 (1997); A. Lasanta and A. Puglisi, *ibid.* **143**, 064511 (2015).

[17] N. Anento and J. A. Padró, Phys. Rev. B **62**, 11428 (2000).

[18] N. Anento and J. A. Padró, Phys. Rev. E **64**, 021202 (2001).

[19] N. Anento, L. E. González, D. J. González, Y. Chushak, and A. Baumketner, Phys. Rev. E **70**, 041201 (2004).

[20] T. Bryk and I. Mryglod, Phys. Rev. E **62**, 2188 (2000).

[21] T. Bryk and I. Mryglod, J. Phys.: Condens. Matter **12**, 6063 (2000).

[22] T. Bryk and I. Mryglod, J. Phys.: Condens. Matter **14**, L445 (2002).

[23] T. Bryk and I. Mryglod, J. Phys.: Condens. Matter **17**, 413 (2005).

[24] A. Verdaguer and J. A. Padró, J. Chem. Phys. **114**, 2738 (2001).

[25] M. M. G. Alemany, J. Souto-Casares, L. E. González, and D. J. González, J. Mol. Liq. **344**, 117775 (2021).

[26] W. B. Street, *Proc. International Cryogenic Engineering Conference 2* (ISTP, London, UK, 1968), p. 260.

[27] V. A. Rabinovich, A. A. Vasserman, V. I. Nedostup, and L. S. Veksler, *Thermophysical Properties of Neon, Argon, Krypton and Xenon* (National Reference Data Service, Moscow, 1976), Vol. 10.

[28] I. A. Richardson, J. W. Leachman, and E. W. Lemmon, J. Phys. Chem. Ref. Data **43**, 013103 (2014).

[29] H. M. Roder, G. E. Childs, R. D. McCarty, and P. E. Angerhofer, *Survey of the Properties of Hydrogen Isotopes Below Their Critical Temperatures*, National Bureau of Standards Technical Note 641 (U.S. Government Printing Office, Washington, D.C., 1973).

[30] D. Güsewell, F. Schmeissner, and J. Schmid, Cryogenics **10**, 150 (1970).

[31] S. R. Challa and J. K. Johnson, J. Chem. Phys. **111**, 724 (1999).

[32] D. A. Keen, J. Appl. Crystallogr. **34**, 172 (2001).

[33] J. Cao and G. A. Voth, J. Chem. Phys. **100**, 5106 (1994).

[34] I. R. Craig and D. E. Manolopoulos, J. Chem. Phys. **121**, 3368 (2004).

[35] H. Kim, Chem. Phys. Lett. **436**, 111 (2007).

[36] J. J. Morales and M. J. Nuevo, J. Comput. Chem. **16**, 105 (1995).

[37] M. Faubel, F. A. Gianturco, F. Ragnetti, L. Y. Rusin, F. Sondermann, U. Tappe, and J. P. Toennies, J. Chem. Phys. **101**, 8800 (1994).

[38] I. F. Silvera and V. V. Goldman, J. Chem. Phys. **69**, 4209 (1978).

[39] U. Balucani and M. Zoppi, *Dynamics of the Liquid State* (Clarendon, Oxford, UK, 1994).

[40] A. Rahman, K. S. Singwi, and A. Sjölander, Phys. Rev. **126**, 986 (1962).

[41] B. J. Braams, T. F. Miller, and D. E. Manolopoulos, Chem. Phys. Lett. **418**, 179 (2006).

[42] D. Levesque and L. Verlet, Phys. Rev. A **2**, 2514 (1970).

[43] The coefficient of kurtosis can be defined in various ways. Here we have introduced the so-called "population kurtosis" γ, which is given by the ratio between the fourth central moment and the squared variance of a probability density distribution, minus three. In this way, $\gamma = 0$ for a Gaussian distribution. See, for example, R. S. King and B. Julstrom, *Applied Statistics Using the Computer* (Alfred Publishing Company, Sherman Oaks, CA, 1982).

[44] P. S. Damle, A. Sjölander, and K. S. Singwi, Phys. Rev. **165**, 277 (1968).

[45] W. T. Coffey and M. W. Evans, Mol. Phys. **35**, 975 (1978).

[46] The Ar sample studied in A. Rahman, Phys. Rev. **136**, A405 (1964) has been newly simulated by the authors of the present paper in the same conditions used in this reference.

[47] E. Guarini, M. Neumann, S. Bellissima, D. Colognesi, and U. Bafile, Phys. Rev. E **100**, 062111 (2019).

[48] E. Guarini, M. Neumann, U. Bafile, S. Bellissima, and D. Colognesi, Phys. Rev. Lett. **123**, 135301 (2019).

[49] E. Guarini, S. Bellissima, U. Bafile, E. Farhi, A. De Francesco, F. Formisano, and F. Barocchi, Phys. Rev. E **95**, 012141 (2017).

[50] S. Bellissima, M. Neumann, E. Guarini, U. Bafile, and F. Barocchi, Phys. Rev. E **92**, 042166 (2015).

[51] S. Bellissima, M. Neumann, E. Guarini, U. Bafile, and F. Barocchi, Phys. Rev. E **95**, 012108 (2017).

[52] F. Barocchi and U. Bafile, Phys. Rev. E **87**, 062133 (2013).

[53] G. P. Srivastava, *The Physics of Phonons*, 2nd ed. (CRC Press, Boca Raton, FL, 2022).

[54] E. Guarini, M. Neumann, A. De Francesco, F. Formisano, A. Cunsolo, W. Montfrooij, D. Colognesi, and U. Bafile, Phys. Rev. E **107**, 014139 (2023).

[55] A. Cunsolo, G. Pratesi, R. Verbeni, D. Colognesi, C. Masciovecchio, G. Monaco, G. Ruocco, and F. Sette, J. Chem. Phys. **114**, 2259 (2001).

[56] E. Guarini, F. Barocchi, A. De Francesco, F. Formisano, A. Laloni, U. Bafile, M. Celli, D. Colognesi, R. Magli, A. Cunsolo, and M. Neumann, Phys. Rev. B **104**, 174204 (2021).

[57] E. W. Lemmon, M. O. McLinden, and D. G. Friend, *Thermophysical Properties of Fluid Systems*, NIST Chemistry WebBook, NIST Standard Reference Database No. 69, edited by P. J. Linstrom and W. G. Mallard (National Institute of Standards and Technology, Gaithersburg, MD, 2017).

[58] S. C. Althorpe, Eur. Phys. J. B **94**, 155 (2021).

[59] K. S. Singwi and M. P. Tosi, Phys. Rev. **149**, 70 (1966).

[60] G. Casanova, A. Levi, and N. Terzi, Physica **30**, 937 (1964).

[61] R. Sharma, K. Tankeshwar, and K. C. Sharma, Phys. Rev. E **59**, 460 (1999).

[62] P. Mausbach, A. Köster, G. Rutkai, M. Thol, and J. Vrabec, J. Chem. Phys. **144**, 244505 (2016).